Università degli studi di Padova

Facoltà di Scienze MM. FF. NN.

Dipartimento di Fisica "G. Galilei"

# DOTTORATO DI RICERCA IN FISICA

XX ciclo

***The OPERA experiment: automated development of nuclear emulsions, installation and results of the Padova microscope***

Coordinatore: *Ch.mo Prof. Attilio Stella*

Supervisore: *Ch.mo Prof. Luca Stanco*

Dottorando: *Enrico Carrara*

31 Gennaio 2008

*...to the dear memory*

*of my grandparents*

*Antonio and Regina...*

## Riassunto

L'esperimento OPERA ha l'obiettivo di verificare l'oscillazione dei neutrini attraverso la misura diretta dell'apparizione di $\nu_\tau$ in un fascio inizialmente puro di $\nu_\mu$ prodotto al CERN. Il suo bersaglio sarà composto da circa 160000 *bricks* di emulsioni nucleari intervallati con lastrine di piombo di 1 mm di spessore. La massa totale dell'esperimento sarà di circa 1.3 kton. Il primo *run* di fisica è avvenuto nell'ottobre 2007, quando sono stati registrati 38 eventi di interazione di $\nu_\mu$.

Durante i 5 anni di vita previsti, OPERA estrarrà per l'analisi circa il 15% del totale delle emulsioni presenti. Queste lastre dovranno essere sviluppate presso i laboratori del Gran Sasso ad un ritmo di circo 20÷30 *brick* al giorno, per 200 giorni l'anno e quindi analizzati al microscopio nel laboratori di OPERA in tutto il mondo. La quantità impressionante di emulsioni da processare ed analizzare richiede uno sviluppo chimico automatizzato su larga scala ed un sistema di acquisizione al microscopio assistito da computer.

Questa tesi di dottorato riporta il mio lavoro nella progettazione e produzione del *software* di controllo per il sistema di sviluppo automatico delle emulsioni e quello sulla stazione di *scanning* presso i laboratori di Legnaro.

Riguardo al primo progetto, ho studiato la miglior struttura del *software* per fornire flessibilità e facilità di mantenimento del codice. Il programma realizzato offre lo *scheduling* ottimale per un numero arbitrario di *brick* sviluppati contemporaneamente sulla linea automatizzata.

Il secondo progetto ha richiesto la completa installazione, messa a punto e verifica del sistema di *scanning*. L'obiettivo, raggiunto con successo, era la ricostruzione di una interazione di neutrino all'interno di uno dei 38 brick di OPERA estratti durante il primo *run* di fisica.

## Abstract

The OPERA experiment aim is to verify the neutrino oscillation, directly measuring the appearance of $\nu_\tau$ from an initially almost pure $\nu_\mu$ beam produced at CERN. Its target will be made of about 160000 *bricks* of nuclear emulsion films sandwiched with 1-mm-thick lead plates. The total mass of the experiment will be of about 1.3 kton. The first physics run has been available in October 2007, when 38 $\nu_\mu$ events have been recorded.

During its expected 5-year lifetime, OPERA will extract for analysis about 15% of the total amount of emulsions. These films need to be developed at LNGS laboratories at the rate of 20÷30 bricks per day, 200 days per year and then scanned by microscope stations in the OPERA laboratories worldwide. The impressive amount of emulsions to be processed and analyzed require automated large-scale chemical development and computer-driven optical scanning.

This Ph.D. thesis reports my job on the design and production of the control software for the automatic emulsion development system and on the automatic scanning station installed at LNL laboratories.

Concerning the former project, I have studied the best software structure to provide flexibility and ease of maintenance for the code. The realized program provides optimal scheduling of any number of bricks simultaneously developed on the automated lines.

The latter project involved the full installation, setting-up and testing of the scanning system. The goal, that has been successfully achieved, was the full reconstruction of a neutrino interaction inside one of the 38 OPERA brick extracted during the first physics run.

# Contents

# Introduction

The neutrino was first postulated in December 1930 by Wolfgang Pauli[1] to explain conservation of energy in beta decay, the decay of a neutron into a proton and an electron. Since then, they have been one of the most challenging and interesting particles known by physicists. In 1956 Clyde Cowan, Frederick Reines, F. B. Harrison, H. W. Kruse, and A. D. McGuire published the article "Detection of the Free Neutrino: a Confirmation"[2] in Science, a result that was rewarded with the 1995 Nobel Prize. The name neutrino was coined by Enrico Fermi, who developed the first theory describing neutrino interactions involved in beta decay[3]. In the Standard Model[4] (SM) there are three neutrinos flavours ($\nu_e, \nu_\mu, \nu_\tau$), each associated to one of the three charged leptons: electron, muon, tauon. In this picture, the neutrinos are considered massless, left-handed particles.

In the last decades, several experiments studied solar and atmospheric neutrinos: Homestake[5], SNO[6], Super-Kamiokande[7], MACRO to cite the most important ones. Early experiments indicated some discrepancies between the theory of the Standard Model, and the actual measurements. Later experiments identified a phenomenon, called neutrino oscillation, as the source of those mismatches. The evidence of a non-massless neutrino was clear to everyone.

Neutrino oscillations hypothesis was first introduced by Pontecorvo[8] in 1958. This basic idea was later extended to oscillations among different neutrino flavours. Oscillation comes out naturally if the three neutrino flavours have non-degenerate non-zero masses; more technically speaking, if the mass eigenstates differ from the weak-interaction eigenstates. As a result, each neutrino is a superposition of different types of neutrinos and therefore the oscillation arises.

The so called "solar neutrino problem", that is the measured deficit in the electronic neutrino flux coming from the Sun to Earth surface[5], has found a good explanation assuming neutrino flavour oscillations in matter with a mass square difference parameter $\Delta m^2$ of the order of $10^{-5}$ eV$^2$ and a relatively large mixing angle between mass and flavour eigenstates.

In the same manner the atmospheric anomaly is interpreted as due to $\nu_\mu \rightarrow \nu_\tau$ oscillations although a direct observation of the $\nu_\tau$ appearance is still missing.

The OPERA (Oscillation Project with Emulsion-tRacking Apparatus) detector is located in the underground National Gran Sasso Laboratory, property of the Italian Institute of Nuclear Physics (INFN). OPERA is an experiment mainly

designed to perform the first detection of neutrino oscillations in appearance mode. The apparatus is placed along the high-energy, long-baseline CERN to LNGS beam (CNGS) at a distance of 730 km from the neutrino source.

OPERA is a hybrid detector made of electronic subdetectors and lead/nuclear emulsion target. The target is composed of Emulsion Cloud Chambers (ECC), whose unit is called *brick*. Each brick is formed of 57 double sided nuclear emulsion films interleaved with 56 1-mm-thick lead plates. The total nominal mass of the experiment exceeds 1.5 kTon, which is required to reach the desired sensitivity in the parameters to be measured. The electronic modules are charged particles trackers and muon spectrometers that accomplish the task of identifying in real time the position of the neutrino/lead interaction inside the target and measure the momentum of the produced muon. When a neutrino hits the detector, the electronics show in which brick the event occurred. The brick is then removed from the experiment's target, the emulsions are chemically developed and sent to the scanning laboratories for interaction vertex analysis. The scanning stations use high-performance automated microscopes for the identification of the tracks inside the emulsions.

The main subjects of this thesis are the description of the emulsion development facility set-up at Gran Sasso laboratories and the set-up, tuning and first results obtained with the automated microscope used in the Padova OPERA group.

This thesis is organized as follows:

The first chapter summarizes the theory of neutrino oscillations in vacuum and in matter.

The second chapter describes the OPERA experiment and the CNGS neutrino beam.

The third chapter describes in more detail the emulsions and their development at the automated facility.

The forth chapter describes the set-up and tuning of the OPERA automated microscope installed at Legnaro laboratories (LNL).

The fifth chapter presents the scanning results obtained with the microscope, scanning real OPERA bricks.

# Chapter 1

# Neutrino masses and oscillations

The neutrino was postulated by Wolfgang Pauli[1] while he was working on the beta decay of nuclei. He assumed a neutrino was emitted together with an electron in the beta decay to explain the continuum energy spectrum of the latter particle while conserving both energy and angular momentum.

The Standard Model electroweak theory, developed in the late 1960's [4], provided a theoretical framework to incorporate neutrinos as left-handed (LH) partners of the charged leptons. In particular, neutrinos were thought to be massless, following the so-called two-component theory of Landau [40] and Lee and Yang [41], in which the massless neutrinos are described by left-handed Weyl spinors. This description has been reproduced in the Standard Model assuming the non existence of right-handed (RH) neutrino fields, which are necessary in order to generate Dirac neutrino masses with the same Higgs mechanism that generates the Dirac masses of quarks and charged leptons[9].

After the successes of the Big Bang nucleosynthesis (BBN) theory and the discovery of the Cosmic Microwave Background[10], it became clear that neutrinos could have played a major role in the history of the early universe and its evolution. The increasing evidence for the existence (and dominance) of dark matter in the universe led to the hypothesis that neutrinos, with small but finite mass, could provide at least part of the dark matter mass. This possibility determined large experimental efforts on the issue of neutrino mass and its role in cosmology, and provided substantial impetus to a worldwide program of experiments addressing the measurement of finite neutrino mass and the possibility of mixing between lepton families (oscillation).

Although it now appears that neutrinos are not to be accounted for the main source of dark matter in the universe, the experimental evidence obtained in the last decade for finite neutrino mass and mixing between generations is strong, and leaves little room to a non-oscillating neutrino description of nature.

The existence of neutrino oscillations requires a change in the Standard Model in order to include three massive neutrinos, three mixing angles and one Dirac-type CP-phase[1]. If neutrinos are Majorana particles[2], two additional Majorana phases are to be included in the matrix which describes this particular extension of the Standard Model.

Neutrinos are peculiar because experiments pose upper limits to their masses which are at least five orders of magnitude smaller than the mass of the corresponding leptons. The most popular explanation of the small neutrino masses is the "seesaw mechanism" in which the neutrino masses are inversely proportional to some large mass scale[3]. If that explanation of the small neutrino mass is true, then the experimentally observed neutrinos are Majorana particles (i.e. indistinguishable from their own antiparticles), and hence the total lepton number is not conserved.

## 1.1 The neutrino mass term

In a field theory the mass of a particle is determined by the mass term in the Lagrangian that describes the particle's interactions. Let us try to extend the SM to accommodate a nonzero mass for neutrinos in the same way that the SM already accommodates nonzero masses for quarks and charged leptons. The latter masses are all of Dirac type and arise from Yukawa coupling, whose vacuum expectation value $\langle\varphi\rangle_0$ yields a term:

$$-f_q \langle\varphi\rangle_0 \overline{q}_L q_R + h.c. \tag{1.1}$$

This is a Dirac mass term for the quark $q$, and $f_q \langle\varphi\rangle_0$ is the corresponding mass. Extending the SM to include neutrino masses is similar to the mechanism just described for the masses of the quarks (and charged leptons), by adding to the model a right-handed neutrino field $\nu_R$ and a Yukawa coupling $-f_\nu \varphi \overline{\nu}_L \nu_R + h.c.$, where $f_\nu$ is a suitable coupling constant. When $\varphi$ develops its vacuum expectation value, this coupling will yield a Dirac mass term

$$\mathcal{L}_D = -f_\nu \langle\varphi\rangle_0 \overline{\nu}_L \nu_R + h.c. \tag{1.2}$$

which provides a neutrino mass $m_\nu = f_\nu \langle\varphi\rangle_0$.

In 1937 Majorana [42] discovered that a massive neutral fermion such as a neutrino can be described by a spinor $\psi$ with only two independent components

[1] CP is the product of two symmetries: C for charge conjugation, which transforms a particle into its antiparticle, and P for parity, which creates the mirror image of a physical system.

[2] Named after the Italian physicist Ettore Majorana. A Majorana fermion is a fermion which coincides with its own anti-particle.

[3] This model produces a light neutrino, corresponding to the three known neutrino flavours, and a very heavy, undiscovered sterile neutrino.

imposing the so-called Majorana condition:

$$\psi = \psi^c \tag{1.3}$$

where $\psi^c = C\overline{\psi}^T$ is the operation of charge conjugation ($C$ is the charge conjugation matrix).

It can be shown that the right-handed component $\psi_R$ of a Majorana neutrino field $\psi$ is not independent from the left-handed component ($\psi_R = \psi_L^c$ and vice-versa). The Majorana field can be re-expressed as

$$\psi = \psi_L + \psi_L^c = \psi_R^c + \psi_R \tag{1.4}$$

A Majorana mass term may be constructed out of $\nu_L$ alone, in which case we have "left-handed Majorana mass":

$$\mathcal{L}_{M_L} = -\frac{m_L}{2}\overline{\nu}_L^c \nu_L + h.c. \tag{1.5}$$

or out of $\nu_R$ alone, in which case we have the "right-handed Majorana mass"

$$\mathcal{L}_{M_R} = -\frac{m_R}{2}\overline{\nu}_R^c \nu_R + h.c. \tag{1.6}$$

An electrically charged fermion cannot have a Majorana mass term, because such a term would convert it into an antifermion, in violation of electric charge conservation. However, for electrically neutral neutrinos, once the field $\nu_R$ exists, there is nothing in the SM that prohibits the occurrence of a right-handed Majorana mass term: such a term does not violate neither the conservation of weak isospin nor that of electric charge. Consequently, if nature contains a Dirac neutrino mass term, then it is likely that it contains a Majorana mass term as well. And, needless to say, if the neutrino does not contain a Dirac neutrino mass term, then it certainly contains a Majorana mass term, which would then be the only source of neutrino mass.

Suppose that a neutrino has a Dirac mass, like for quarks and charged leptons, and also a right-handed Majorana mass as in (1.6). Its total mass term $\mathcal{L}_{m_\nu}$ is then

$$\begin{aligned} \mathcal{L}_{m_\nu} &= -m_D \overline{\nu}_R \nu_L - (m_R/2)\overline{\nu}_R^c \nu_R + h.c. \\ &= -\tfrac{1}{2}\left[\overline{\nu}_L^c, \overline{\nu}_R\right] \begin{bmatrix} 0 & m_D \\ m_D & m_R \end{bmatrix} \begin{bmatrix} \nu_L \\ \nu_R^c \end{bmatrix} + h.c. \end{aligned} \tag{1.7}$$

The matrix $\mathcal{M}_\nu$

$$\mathcal{M}_\nu = \begin{bmatrix} 0 & m_D \\ m_D & m_R \end{bmatrix} \tag{1.8}$$

appearing in $\mathcal{L}_{m_\nu}$ is called the neutrino mass matrix.

## 1.2 The seesaw mechanism

It is natural to assume that the neutrino Dirac mass $m_D$ is of the same order of magnitude as the Dirac masses of the quarks and charged leptons, since in the SM all Dirac masses arise from coupling to the same Higgs field. The Dirac masses of the quarks and charged leptons are their total masses, so we expect $m_D$ to be of the same order of magnitude as the mass of a typical quark or charged lepton. Furthermore, since nothing in the SM requires the right-handed Majorana mass $m_R$ to be small, one may expect that this mass could be "large": $m_R \gg m_D$.

The mass matrix $\mathcal{M}_\nu$ can be diagonalized by the transformation

$$Z^T \mathcal{M}_\nu Z = \mathcal{D}_\nu \tag{1.9}$$

where

$$\mathcal{D}_\nu = \begin{bmatrix} m_1 & 0 \\ 0 & m_2 \end{bmatrix} \tag{1.10}$$

is a diagonal matrix whose diagonals elements are the positive-definite eigenvalues of $\mathcal{M}_\nu$, $Z$ is a unitary matrix and $T$ denotes transposition.

To order $\rho^2$ of the small parameter $\rho \equiv m_D/m_R$:

$$\mathcal{D}_\nu = \begin{bmatrix} m_D^2/m_R & 0 \\ 0 & m_R \end{bmatrix} \tag{1.11}$$

Thus the mass eigenvalues are $m_1 \simeq m_D^2/m_R$ and $m_2 \simeq m_R$.

To express $\mathcal{L}_{m_\nu}$ in terms of mass eigenfields, we define the two-component column vector $\nu_L$ by

$$\nu_L \equiv Z^{-1} \begin{bmatrix} \nu_L \\ \nu_R^c \end{bmatrix} \tag{1.12}$$

(The column-vector field $\nu_L$ is chirally left-handed, since by definition the charge conjugate of a field with a given chirality always has the opposite chirality.) We then define the two-component field $\nu$, with components $\nu_{light}$ and $\nu_{heavy}$, by

$$\nu \equiv \nu_L + \nu_L^c \equiv \begin{bmatrix} \nu_{light} \\ \nu_{heavy} \end{bmatrix} \tag{1.13}$$

(the meaning of the subscripts *light* and *heavy* will become clear in the following). Using the fact that scalar covariant combinations of fermion fields can connect only fields of opposite chirality, the $\mathcal{L}_{m_\nu}$ of (1.7) may be rewritten as

$$\mathcal{L}_{m_\nu} = -\sum_{i=light}^{heavy} \frac{m_i}{2}\, \overline{\nu}_i\, \nu_i + h.c. \tag{1.14}$$

We recognize the $i$-th term of this expression as the mass term for a neutrino $\nu_i$.

From the definition (1.13), $\nu_i = \nu_{Li} + \nu_{Li}^c$ goes into itself under charge conjugation. A neutrino whose field has this property is identical to its antiparticle,

and is known as a Majorana neutrino. Thus, the eigenstates of the combined Dirac-Majorana mass term $\mathcal{L}_{m_\nu}$ of (1.7) are Majorana neutrinos.

As we have seen, with $m_D$ of the order of the mass of a typical quark or charged leptons, and $m_R \gg m_D$, the mass of $\nu_{light}$,

$$m_{light} \cong m_D^2/m_R \tag{1.15}$$

can be very small. Thus, if we define $\nu_{light}$ as one of the light neutrinos, we have an elegant explanation of why it is so light. This explanation, in which physical neutrino masses are so small because the right-handed Majorana mass $m_R$ is large, is known as the *see-saw mechanism*, and (1.15) is referred to as the see-saw relation [12]. The mass $m_R$ is assumed to reflect some high mass scale where new physics responsible for neutrino mass resides. Interestingly, if $m_R$ is just a little below the grand unification scale, e.g. $m_R \sim 10^{15}$ GeV, and $m_D \sim m_{top} \simeq 175$ GeV, then from the see-saw relation (1.15) we obtain $m_{light} \sim 3 \times 10^{-2}$ eV. This is in the range of neutrino mass suggested by the experiments on atmospheric neutrino oscillations.

Under these assumptions about $m_D$ and $m_R$, the mass of $\nu_{heavy}$ is very large

$$m_{heavy} \cong m_R \tag{1.16}$$

The eigenstate $\nu_{heavy}$ cannot be one of the light neutrinos, but is an hypothetical very heavy neutral lepton. Such neutral leptons are candidates to explain the baryon-antibaryon asymmetry of the Universe.

The seesaw mechanism predicts that light neutrinos such as $\nu_{light}$, as well as the hypothetical heavy neutral leptons such as $\nu_{heavy}$, are Majorana particles. The prediction of light neutrinos of this model is one of the factors driving a major effort to look for neutrinoless double beta decay[13]. This is the $L-$violating decay $A \to A^{'} + 2e^{-}$ in which one nucleus decays into another plus two electrons, with no emission of neutrinos. The observation of this reaction would show that the light neutrinos are indeed Majorana particles [14].

## 1.3 Three-neutrino mixing

So far, we have analyzed the simplified case in which there is only one light neutrino and one heavy neutral lepton. In the real world, there are three leptonic generations, with a light neutrino in each one. The analysis could be extended to accommodate this situation.[4]

In the SM, there are left-handed weak-eigenstate charged leptons $l_{L\alpha}$, where $\alpha = e, \mu$, or $\tau$. Each of them couples to an LH weak-eigenstate neutrino $\nu_{L\alpha}$, via

[4]For simplicity, the possibility with light sterile (non-interacting) neutrinos in addiction to the three light active ones is not included. Experimentally, stringent limits on sterile neutrino contributions to atmospheric neutrino oscillations have been obtained [11].

the charged-current weak interaction

$$\mathcal{L}_W = -(g/\sqrt{2})W_\rho^- \sum_{\alpha=e,\mu,\tau} \bar{l}_{L\alpha}\gamma^\rho \nu_{L\alpha} + h.c. \tag{1.17}$$

Here, $W_\rho$ are the charged weak bosons and $g$ is the weak coupling constant. To allow for neutrino masses, we add to the model the RH fields $\nu_{R\alpha}$, where $\alpha = e, \mu$, or $\tau$. Then, in analogy with (1.7), we introduce the neutrino mass term

$$\mathcal{L}_{m_\nu} = -\frac{1}{2}\left[\overline{\nu}_L^c, \overline{\nu}_R\right] \begin{bmatrix} 0 & m_D^T \\ m_D & m_R \end{bmatrix} \begin{bmatrix} \nu_L \\ \nu_R^c \end{bmatrix} + h.c. \tag{1.18}$$

In this case, $\nu_L$ is the column vector

$$\nu_L \equiv \begin{bmatrix} \nu_{Le} \\ \nu_{L\mu} \\ \nu_{L\tau} \end{bmatrix} \tag{1.19}$$

and similarly for $\nu_R$. The quantities $m_D$ and $m_R$ are now $3 \times 3$ matrices. Since the matrix $m_R$ may be taken to be symmetric, the $6 \times 6$ mass matrix

$$\mathcal{M}_\nu = \begin{bmatrix} 0 & m_D^T \\ m_D & m_R \end{bmatrix} \tag{1.20}$$

is also symmetric. Such a matrix may be diagonalized by the transformation in (1.9), but where $Z$ is a $6 \times 6$ unitary matrix and $\mathcal{D}_\nu$ is a $6 \times 6$ diagonal matrix whose diagonal elements $m_i$, $i = 1, ..., 6$, are positive-definite eigenvalues of the $\mathcal{M}_\nu$ defined in (1.20).

It can be shown, as before, that after diagonalization the mass term $\mathcal{M}_\nu$ of (1.18) may be rewritten as

$$\mathcal{L}_{m_\nu} = -\sum_{i=1}^{6} \frac{m_i}{2} \overline{\nu}_i \nu_i + h.c. \tag{1.21}$$

Thus, the $\nu_i$ are the neutrinos of definite mass $m_i$, where each $\nu_i$ is a Majorana neutrino.

From experimental searches for heavy neutral leptons, we know that there are none with masses below 80 GeV [43]. Thus, in neutrino experiments at lower energies (and even at much higher energies if the heavy neutrinos are at the TeV or at the grand unification scale), it is only the light neutrinos that play a significant role.

Now from the $6 \times 6$ analogue of (1.12) and an appropriate diagonalization matrix Z:

$$Z = \begin{bmatrix} V & Y \\ X & W \end{bmatrix} \tag{1.22}$$

where V, Y, X, W are 3 *times* 3 submatrices, one can write:

$$\nu_{L\alpha} = \sum_{i=1}^{3} \left( V_{\alpha i} \nu_{Li}^{light} + Y_{\alpha i} \nu_{Li}^{heavy} \right) \cong \sum_{i=1}^{3} V_{\alpha i} \nu_{Li}^{light} \tag{1.23}$$

where we have used $V \gg Y$ in the second step. This scenario, called *three-neutrino mixing* can accommodate the experimental evidences of neutrino oscillations in solar and atmospheric neutrino experiments.

From (1.23), we may rewrite the weak interaction (1.17) as

$$\mathcal{L}_W \cong -\frac{g}{\sqrt{2}} W_\rho^- \bar{l}_L \gamma^\rho U \nu_L^{light} - \frac{g}{\sqrt{2}} W_\rho^+ \overline{\nu}_L^{light} \gamma^\rho U^+ l_L \tag{1.24}$$

Here,

$$U \equiv A_L^+ V \tag{1.25}$$

is the "leptonic mixing matrix" called PMNS matrix to honor the pioneering contributions of Pontecorvo, Maki, Nakagawa, Sakata [46].

Equation (1.24) expresses the charged-current weak interaction in terms of charged leptons and neutrinos of definite mass. Since the matrix $Z$ is unitary, and $X$ and $Y$ are much smaller than $V$ and $W$, the matrix $V$ is to a good approximation unitary itself. From the unitarity of $A_L$ and (1.25), this means that the leptonic mixing $U$ is approximately unitary as well.

The matrix $U$ has nine entries, each of which may have a real and an imaginary part, leading to a total of 18 parameters. On these parameters, unitary imposes nine constraints. First of all, each of the three columns of $U$ must be a vector of unit length. Secondly, any two columns must be orthogonal to each other. This requirements lead to three orthogonality conditions, each of which has a real and an imaginary part, for a total of six constraints. With the nine unitary constraints taken into account, nine parameters are left which can be divided in three mixing angles and six phases. However, only three phases are physical.

These three phases are usually denominated by $\alpha_1$, $\alpha_2$ and $\delta$, where the former two are usually called "Majorana phases", because they appear only if the massive neutrinos are Majorana particles. The phase $\delta$ is usually called "Dirac phase", because it is present also if the massive neutrinos are Dirac particles, being the analogous of the phase in the quark mixing matrix. These complex phases in the mixing matrix generate violations of the CP symmetry.

## 1.4 Neutrino flavor change in vacuum

Neutrino flavor change in vacuum is the oscillation process in which a neutrino is created together with a charged lepton $l_\alpha$ of flavor $\alpha$, then travels a macroscopic distance $L$ in vacuum, and finally interacts with a target to produce a second charged lepton $l_\beta$ whose flavor $\beta$ is different from that of the first charged lepton. The intermediate neutrino can be any of the (light) mass eigenstates $\nu_i$, and the

amplitude for the oscillation is the coherent sum of the contributions of the various mass eigenstates. The contribution of a given $\nu_i$ is a product of three factors: the amplitude $U^*_{\alpha i}$ of the created $\nu_\alpha$ to be the mass eigenstate $\nu_i$, the amplitude for this $\nu_i$ with $E$ energy to travel a distance $L$ is $\exp(-im_i^2 L/2E)$ [44], and last the amplitude $U_{\beta i}$ for $\nu_i$, having arrived at the target, to produce the particular charged lepton $l^-_\beta$. Thus the amplitude $Amp\,[\nu_\alpha \to \nu_\beta]$ for $\nu_\alpha \to \nu_\beta$ oscillation is given by

$$Amp\,[\nu_\alpha \to \nu_\beta] = \sum_i U^*_{\alpha i} e^{-im_i^2(L/2E)} U_{\beta i} \tag{1.26}$$

where the sum runs over all the light mass eigenstates. Squaring this relation and using the (at least approximate) unitary of the mixing matrix $U$, we find that the probability $P(\nu_\alpha \to \nu_\beta)$ for $\nu_\alpha \to \nu_\beta$ oscillation is given by [44].

$$\begin{aligned} P(\nu_\alpha \to \nu_\beta) &= |Amp\,[\nu_\alpha \to \nu_\beta]|^2 = \\ &= \delta_{\alpha\beta} - 4\textstyle\sum_{i>j} Re(U^*_{\alpha i} U_{\beta i} U_{\alpha j} U^*_{\beta j}) \sin^2\left[\Delta m^2_{ij}(L/4E)\right] \\ &\quad + 2\textstyle\sum_{i>j} Im(U^*_{\alpha i} U_{\beta i} U_{\alpha j} U^*_{\beta j}) \sin\left[\Delta m^2_{ij}(L/2E)\right] \end{aligned} \tag{1.27}$$

where $\Delta m^2_{ij} \equiv m^2_i - m^2_j$. This expression for $P(\nu_\alpha \to \nu_\beta)$ is valid for an arbitrary number of neutrino mass eigenstates, and holds whether $\beta$ is different from $\alpha$ or not. If all the neutrino masses, and consequently all the splittings $\Delta m^2_{ij}$, vanish, then $P(\nu_\alpha \to \nu_\beta) = \delta_{\alpha\beta}$. Thus the oscillation in vacuum of $\nu_\alpha$ into a different flavor $\nu_\beta$ implies neutrino masses to be non-degenerate, and in particular non-zero. From (1.26), is clear that this change of flavor also implies neutrino mixing: in the absence of mixing, the matrix $U$ is diagonal so that $Amp\,[\nu_\alpha \to \nu_\beta]$ vanishes if $\beta \neq \alpha$. Finally, Eq. (1.27) shows the sinusoidal form of the oscillation probability as a function of $L/E$, justifying the name "oscillation".

It is worth noting that, up to now, experiments measured only disappearance probabilities (i.e. $\alpha = \beta$ in Eq. 1.27). Even the SNO experiment, which measures the overall flux of three active neutrinos via NC interactions, cannot distinguish different flavors. On the other hand, in the case of OPERA, it will be possible to consider the appearance probability since the appearance of all the active flavors in the beam could be experimentally observed. However, a complete 3-family scheme and a possible CP invariance violation are far away to be measured and, at present, only experimental proposals exist on this subject.

In the simplest case of two neutrino mixing between $\nu_\alpha$, $\nu_\beta$ and $\nu_1$, $\nu_2$, there is only one squared-mass difference $\Delta m = \Delta m^2_{21} = m^2_2 - m^2_1$ and the mixing matrix can be parameterized in terms of one mixing angle $\theta$:

$$U = \begin{bmatrix} \cos\theta & \sin\theta \\ -\sin\theta & \cos\theta \end{bmatrix} \tag{1.28}$$

The resulting survival probability of a given flavor can be written as

$$P(\nu_\alpha \to \nu_\alpha) = 1 - \sin^2 2\theta \sin^2 \left[1.27 \frac{\Delta m^2(eV^2) L(km)}{E_\nu(GeV)}\right] \tag{1.29}$$

where we introduced the correct $c$ and $h$ factors inside the $\sin^2$ argument. This expression is historically very important, because data from solar and atmospheric neutrino experiments have been analyzed (in first approximation) in the two-neutrino mixing framework using Eq. (1.29).

The oscillations in this approximation are characterized by the amplitude $\sin^2 2\theta$ and by the oscillation length

$$L_{osc}(km) = \frac{2.48\ E_\nu(\mathrm{GeV})}{\Delta m^2(\mathrm{eV}^2)} \tag{1.30}$$

An experiment is characterized by the typical neutrino energy $E$ and by the source-detector distance $L$. The ratio $L/E$ establishes the $\Delta m^2$ range to which an experiment is sensitive.

## 1.5 Phenomenology of three neutrino mixing

The evidences of solar and atmospheric neutrino oscillations are nicely accommodated in the minimum framework of three-neutrino mixing, in which the three flavor neutrinos are linear combinations of three neutrino $\nu_1$, $\nu_2$ and $\nu_3$ with masses $m_1$, $m_2$ and $m_3$. In the mixing matrix $U$ (1.25), the mixing angle $\theta_{12}$ is associated with the solar neutrino oscillations, hence the masses $m_1$ and $m_2$ are separated by the smaller interval $\Delta m^2_{solar}$ (we shall assume, by convention, that $m_2 > m_1$) while $m_3$ is separated from the 1, 2 pair by the larger interval $\Delta m^2_{atm}$, and can be either lighter or heavier than $m_1$ and $m_2$. The situation where $m_3 > m_2$ is called "normal hierarchy", while the "inverse hierarchy" has $m_3 < m_1$.

The general formula (1.27) can be simplified in several cases of practical importance. For three neutrino flavors, using the empirical fact that $\Delta m^2_{atm} >> \Delta^2_{sol}$ and considering distances comparable to the atmospheric neutrino oscillation length, only four parameters are relevant at the lowest order of approximation: the angles $\theta_{23}$, $\theta_{13}$ and the parameters $\Delta_{atm} \equiv \Delta m^2_{atm} L/4E_\nu$, $\Delta_{sol} \equiv \Delta m^2_{sol} L/4E_\nu$.

Therefore one can write the disappearance probability of $\nu_\mu$ as

$$\begin{aligned} P(\nu_\mu \to \nu_x) \quad &\approx \sin^2 2\theta_{13} \left[\sin^2 \Delta_{atm} - \Delta_{sol} \sin^2 \theta_{12} \sin 2\Delta_{atm}\right] \\ &+ \Delta^2_{sol} \cos^4 \theta_{13} \sin^2 2\theta_{12} \end{aligned} \tag{1.31}$$

## 1.6 Neutrino oscillations in matter

When neutrinos pass through matter between their source and a target detector, their coherent forward scattering from particles in matter can significantly modify

their oscillation pattern. This is true even if, as in the Standard Model, forward scattering of neutrinos from other particles does not by itself change neutrino flavor. The flavor change in matter that grows out by an interplay between flavor-non changing neutrino-matter interactions and neutrino mass and mixing is know as the Mikheyev-Smirnov-Wolfenstein (MSW) effect [45].

To treat a neutrino in matter, we shall make the simplifying assumption that we are dealing with an effectively "two-neutrino" problem. The neutrino is described by a column vector in flavor space,

$$\begin{bmatrix} a_e(t) \\ a_\mu(t) \end{bmatrix} \tag{1.32}$$

where $a_e(t)$ is the amplitude for the neutrino to be a $\nu_e$ at time $t$, and similarly for the other flavor. The time evolution of the neutrino state is then described by the Schrödinger equation in which the Hamiltonian $\mathcal{H}$ is a $2 \times 2$ matrix that acts on this column vector. If our neutrino is travelling in vacuum, the mixing is described by the vacuum mixing matrix

$$U_V = \begin{bmatrix} \cos\theta_V & \sin\theta_V \\ -\sin\theta_V & \cos\theta_V \end{bmatrix} \tag{1.33}$$

in which $\theta_V$ is the mixing angle in vacuum. $\mathcal{H}$ in vacuum is then

$$\mathcal{H}_V = \frac{\Delta m_V^2}{4E} \begin{bmatrix} -\cos 2\theta_V & \sin 2\theta_V \\ \sin 2\theta_V & cos2\theta_V \end{bmatrix} \tag{1.34}$$

Here, $\Delta m_V^2 \equiv m_2^2 - m_1^2$ is the square of the mass splitting in vacuo, and $E$ is the neutrino energy. The probability $P_V(\nu_e \to \nu_\mu)$ for $\nu_e \to \nu_\mu$ oscillation in vacuo is given by

$$P_V(\nu_e \to \nu_\mu) = \sin^2 2\theta_V \sin^2\left(\Delta m_V^2 \frac{L}{4E}\right) \tag{1.35}$$

In matter, $W$-exchange-induced coherent forward scattering of $\nu_e$ from ambient electrons adds an interaction energy $V$ to the $\nu_e - \nu_e$ element of $\mathcal{H}$. $V$ must be proportional to $G_F$, the Fermi constant, and to $N_e$, the number of electrons per unit volume. It can be shown that [15]

$$V = \sqrt{2} G_F N_e \tag{1.36}$$

Thus, the $2\times2$ Hamiltonian in matter is then

$$\mathcal{H} = \frac{\Delta m_V^2}{4E} \begin{bmatrix} -\cos 2\theta_V & \sin 2\theta_V \\ \sin 2\theta_V & cos2\theta_V \end{bmatrix} + \begin{bmatrix} V & 0 \\ 0 & 0 \end{bmatrix} \tag{1.37}$$

Adding to this $\mathcal{H}$ the multiple $-V/2$ of the identity, we may rewrite it as

$$\mathcal{H} = \frac{\Delta m_M^2}{4E} \begin{bmatrix} -\cos 2\theta_M & \sin 2\theta_M \\ \sin 2\theta_M & cos2\theta_M \end{bmatrix} \tag{1.38}$$

Here,

$$\Delta m^2_M = \Delta m^2_V \sqrt{\sin^2 2\theta_V + (\cos 2\theta_V - x)^2} \tag{1.39}$$

is the effective mass splitting in matter, and

$$\sin^2 2\theta_M = \frac{\sin^2 2\theta_V}{\sin^2 2\theta_V + (\cos 2\theta_V - x)^2} \tag{1.40}$$

is the effective mixing angle in matter. In this expression,

$$x \equiv \frac{V}{\Delta m^2_V / 2E} \tag{1.41}$$

is a dimensionless measure of the relative importance of the interaction with matter in the behavior of the neutrino.

If a neutrino travels through matter of constant density, then $\mathcal{H}$ (1.38) is a position-independent constant. As we can see, it is exactly the same as the vacuum Hamiltonian (1.34), except that the vacuum mass splitting and mixing angle are replaced by their values in matter. As a result, the oscillation probability is given by the Eq. 1.35, but with the mass splitting and mixing angle replaced by their values in matter. The latter values can largely differ from their vacuum counterparts. A striking example is the case where the vacuum mixing angle $\theta_V$ is very small, but $x \cong \cos 2\theta_V$. Then, as we see from Eq. 1.40, $\sin^2 2\theta_M \cong 1$. Interaction with matter has modified a very small mixing angle with a maximal one.

# Chapter 2

# The OPERA experiment

## 2.1 The OPERA experiment

OPERA (**O**scillation **P**roject with **E**mulsion-t**R**acking **A**pparatus) is a long baseline experiment designed primarily to make a conclusive test of the $\nu_\mu \rightarrow \nu_\tau$ oscillation hypothesis by means of the direct observation of $\nu_\tau$ in an initially pure $\nu_\mu$ beam. The beam is produced at CERN, in Geneve, and fired towards the OPERA detector (Fig. 2.1), which is located in the Hall C of the Gran Sasso Underground Laboratory, 730 km away)[22]. The average energy of the neutrinos is above the $\tau$ lepton production threshold, in the oscillation parameter region indicated by atmospheric neutrino experiments.

### 2.1.1 The CNGS neutrino beam

The CNGS[16] neutrino beam was designed and optimized for the study of $\nu_\mu \rightarrow \nu_\tau$ oscillations in appearance mode, by maximizing the number of charged current (CC) $\nu_\tau$ interactions at the LNGS site. A 400 GeV proton beam is extracted from the CERN SPS in 10.5 $\mu$s short pulses with a design intensity of 2.4 x $10^{13}$ proton on target (p.o.t) per pulse. The proton beam is transported through the transfer line TT41 to the CNGS target T40 [23] . The target consists of a series of helium-cooled thin graphite rods. Secondary pions and kaons of positive charge produced in the target are focused into a parallel beam by a system of two magnetic lenses, called horn and reflector.

A 1000 m long decay-pipe allows the pions and kaons to decay into muon-neutrinos and muons. The remaining hadrons (protons, pions, kaons, ... ) are absorbed by an iron beam-dump. The muons are monitored by two sets of detectors downstream of the dump; they measure the muon intensity, the beam profile and its average position. Further downstream the muons are absorbed in the rock while neutrinos continue to travel toward Gran Sasso (Fig. 2.2).

The average neutrino energy at the LNGS location is 17 GeV. The $\bar{\nu}_\mu$ contam-

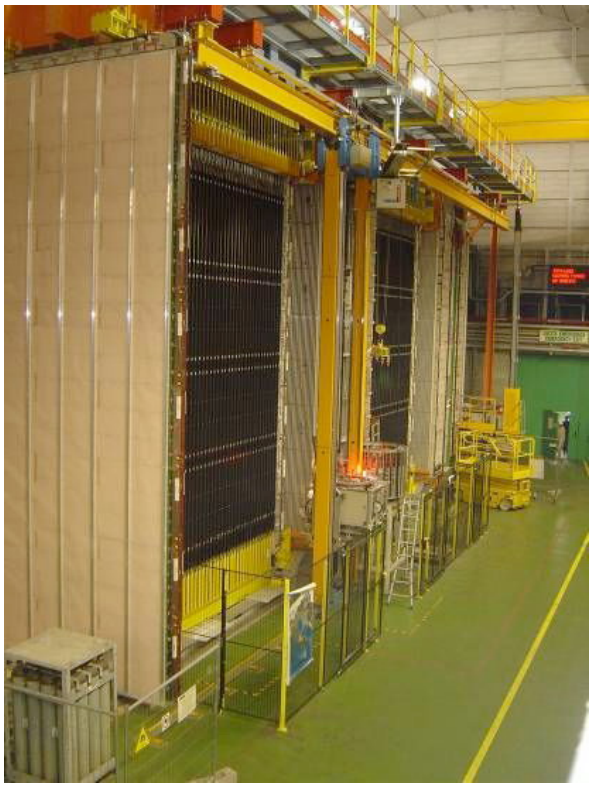

Figure 2.1: Overview of the OPERA experiment in Hall C of the National Laboratories of Gran Sasso.

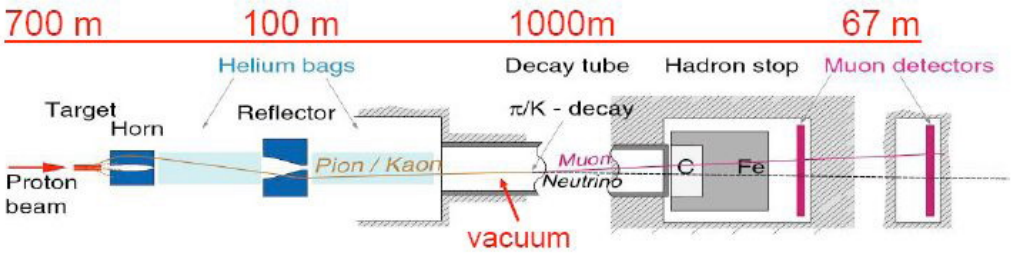


Figure 2.2: Layout of the CNGS beam facility.

ination is 4%, the $\nu_e$ and $\bar{\nu}_e$ contaminations are lower than 1%, while the number of prompt $\nu_\tau$ from $D_s$ decay is negligible. The average $L/E_\nu$ ratio is 43 km GeV$^{-1}$. Due to the Earth curvature neutrinos from CERN enter the LNGS halls with an angle of about 3 degrees with respect to the horizontal plane. Assuming a CNGS beam intensity of 4.5 x $10^{19}$ p.o.t. per year and a five year run, about 31000 charged current (CC) plus neutral current (NC) neutrino events will be collected by OPERA from interactions in the lead-emulsion target. Out of them 95 (214) CC $\nu_\tau$ interactions are expected for $\Delta m^2$ = 2 x $10^{-3}$ eV$^2$ (3 x $10^{-3}$ eV$^2$) and $\sin^2 2\theta_{23} = 1$. Taking into account the overall $\tau$ detection efficiency the experiment should gather $10 \div 15$ signal events with a background of less than one event.

| | |
|---|---|
| $\nu_\mu$(m$^-$2/pot) | $7.36 \times 10^{-9}$ |
| $\nu_\mu$ CC events/pot/kTon | $5.05 \times 10^{-17}$ |
| $\langle$ E $\rangle_{\nu_\mu}$ (GeV) | 17 |
| $\nu_e/\nu_\mu$ | 0.8% |
| $\bar{\nu_\mu}/\nu_\mu$ | 4% |
| $\bar{\nu_e}/\nu_\mu$ | 0.07% |

Table 2.1: The CNGS beam main characteristics.

About 26000 muons per year will be produced in the CC interactions of the $\nu_\mu$ in the rock upstream of OPERA and will eventually hit the experiment (assuming $4.9 \times 10^{19}$ pot at CERN).

### 2.1.2 The detector

The OPERA detector consists of two identical supermodules (SM), longitudinally aligned along the beam axis (Fig. 2.3). Each supermodule is made of a target and a spectrometer.

The target is made of a large number of Emulsion Cloud Chambers (ECCs), commonly called *bricks*. The bricks consist of a lead/emulsion sandwich which provides both large target mass and high precision tracking of charged particles. Bricks are stored in modular vertical arrays called walls. Between each pair of walls the target is instrumented with electronic detectors based on solid scintillator strip technology; these devices are called Target Trackers (TT), see Fig. 2.4.

The spectrometer is placed downstream after the target and consists of several walls of drift tubes and a magnetic dipole, instrumented with gas electronic detectors called Resistive Plate Chambers (RPCs).

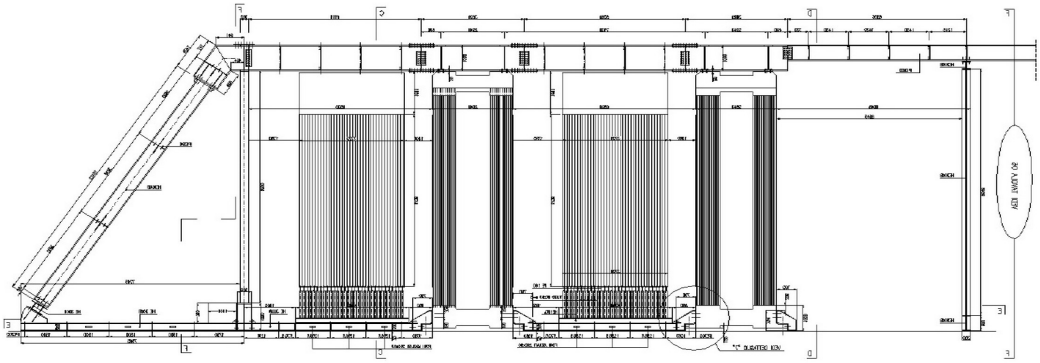

Figure 2.3: Schematic drawing of the OPERA experiment (side view). Neutrino beam comes from left-hand side.

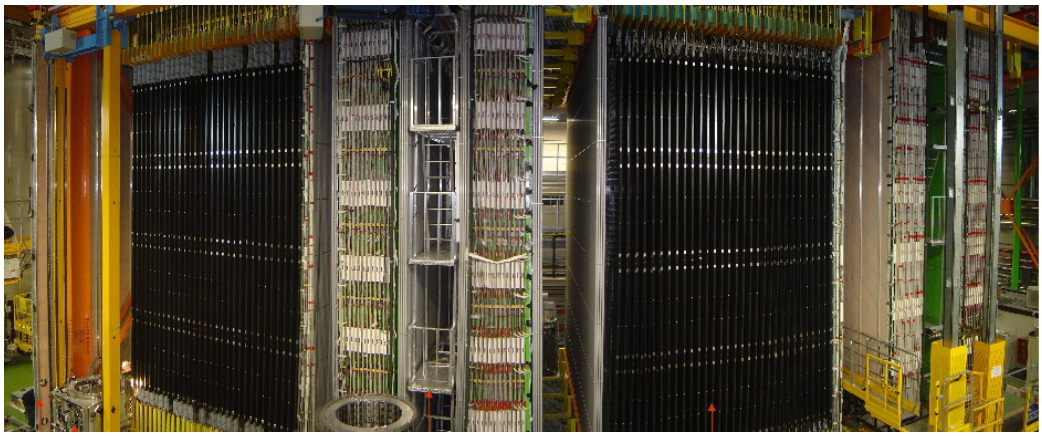

Figure 2.4: View of the OPERA experiment. The two supermodules are visible, the black detectors are the Target Tracker walls, followed by the magnetic spectrometers.

### Emulsion Cloud Chambers (ECC)

The $\nu_\tau$ appearance search is based on the observation of $\tau^-$ events produced by CC interactions, with the $\tau^-$ decaying in all possible decay modes:

$$\begin{aligned} \tau^- &\rightarrow e^- \nu_\tau \overline{\nu}_e \\ \tau^- &\rightarrow \mu^- \nu_\tau \overline{\nu}_\mu \\ \tau^- &\rightarrow h^- \nu_\tau (n\pi^0) \\ \tau^- &\rightarrow 3\pi \nu_\tau \end{aligned} \tag{2.1}$$

Since the expected event rate is small, it is crucial to efficiently separate the $\nu_\tau$ CC events from all the other flavor neutrino events, and to keep the background at a very low level. For this purpose, the detectors will have to identify the event by exploiting the $\tau$ decay specific properties, characterized by a short lifetime and the presence of missing transverse momentum due to the $\nu_\tau$ in the final state.

The basic structure of the emulsion detector is called Emulsion Cloud Chamber (ECC) and is made of ECC *bricks*. Each brick consists of 57 emulsion sheets; in order to have large mass (1.3 kton) and high granularity the emulsion sheets are interleaved with 1 mm thick lead plate. The brick is packed with adesive aluminum foil, to protect the emulsions from external light. At the downstream end of each brick a small plastic box, containing two emulsion sheets, named *Changeable Sheets* (CS) is further attached (Fig. 2.5).

The emulsions used to build ECC are 44$\mu$m-thick layers placed at the upper and bottom surfaces of a 205 $\mu$m-thick plastic base (fig. 2.6).

The CS can be easily removed and analyzed, without opening the whole brick. The information of the CS is used for a precise prediction of the position of the tracks in the most downstream films of the brick, hence guiding the so called scan-back vertex finding procedure. The bricks, produced by the *Brick Assembling Machine* (BAM), are allocated on circular drums that are then handled by the *Brick Manipulator System* (BMS), which is made of two robots each operating at one side of the detector. An arm is used to insert the bricks into the experiment's target. The extraction of a brick, in the region indicated by electronic detectors, is done by a vacuum sucker of the BMS. The dimensions of a brick are 12.5 $\times$ 10.2 $\times$ 7.5 cm$^3$, the weight is 8.3 kg each. In terms of radiations length, a brick corresponds to a thickness of 10 $X_0$ which is long enough to allow the identification of electrons by electromagnetic showers and to measure momentum by multiple Coulomb scattering following the tracks in consecutive emulsion sheets [24].

The process of installing bricks on the walls has started and constantly progressing; when this task will be completed about 160000 bricks will be installed on the walls.

Details on the emulsions and of the techniques of analysis will be given in Chapters 3 and 4.

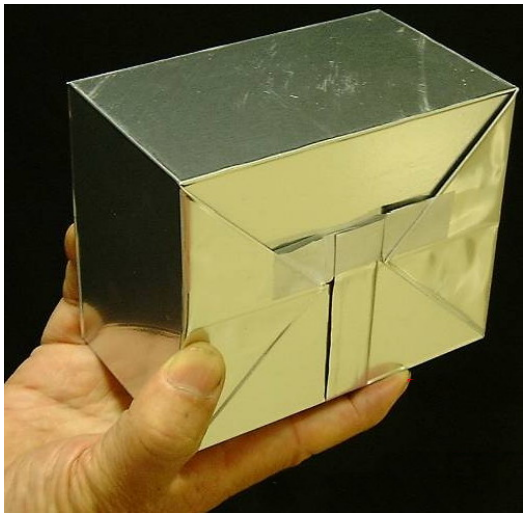

Figure 2.5: ECC brick, basic element of the OPERA target.

### Target Tracker

Between two consecutive lead/emulsion brick walls, electronic detectors trigger the $\nu$ interaction and identify the brick containing the candidate event.

An electronic target tracker module consists of two planes of 6.6 m long scintillator strips in each transverse directions (X and Y, horizontal and vertical) (see Fig. 2.7). The strips, 2.6 cm wide,1 cm thick and 6.8 m long, have Wave Length Shifting (WLS) fibers for readout by 64 multi-anode photomultiplier tubes.

The strips are arranged in read-out units, four of these units cover the whole plane relative to a brick wall. In order to minimize the spatial resolution of the reconstructed interaction back to the bricks, the TT walls are placed at the shortest possible distance (about 3 cm) from the brick walls.

The TT walls are also used as calorimeter, analyzing events by energy sampling of hadronic showers, and helping the tracking of penetrating particles in conjunction with the RPC spectrometers.

Vertex brick identification is made in two subsequent steps: first the right brick wall is identified, then the correct brick in which the even occurred is determined and extracted. The localization efficiency is mainly limited by the *back-scattering* of secondary particles. This is due to particles produced in the neutrino interaction, that re-interact themselves and the resulting products may travel backwards with the respect to the beam direction, causing a mis-identification of the interaction wall or brick. This effect is higher in deeply inelastic events and grows with the energy of the incident neutrino.

Vertex location efficiency depends on whether the event has a muon in the final state or not. In the former case, the vertex finding efficiency is of 94% vertexes found with a spacial resolution of 0.8 cm; in the latter case the efficiency drops to

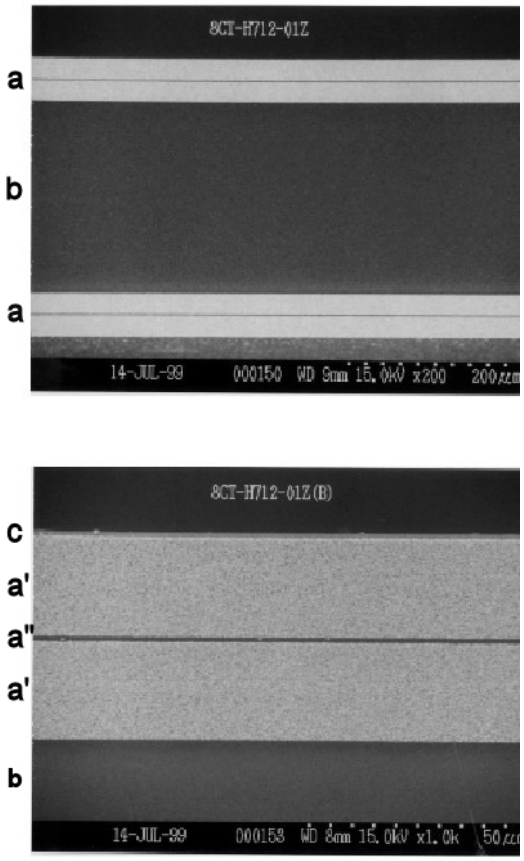


Figure 2.6: Microscope views of an OPERA emulsion. You can clearly see (a) the 44$\mu$m-thick emulsion layers and (b) the 200$\mu$m-thick plastic base. At a greater magnification (c) the 1$\mu$m-thick protective film, (a$'$) the two photographic emulsion coats and (a") the low efficiency conjunction surface.

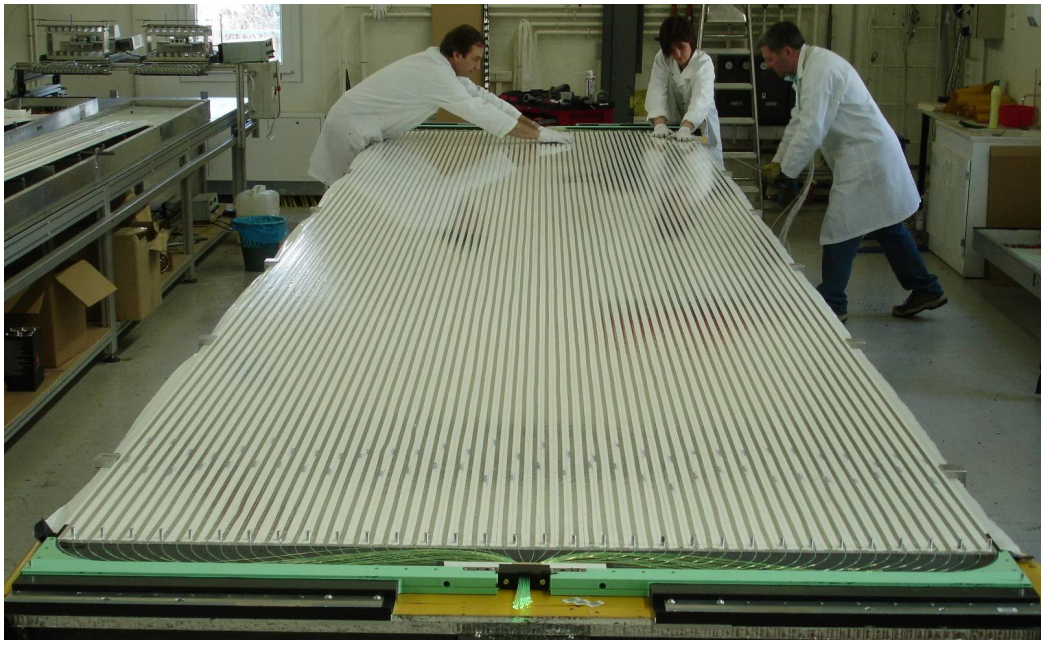

Figure 2.7: Preparation of a Target Tracker module. The termination of the optical fibers is visible in the center, at the bottom of the image.

84%, found with a 1.1 cm resolution. In general terms the vertex finding efficiency depends on the extraction algorithm used, i.e. how many bricks are extracted per event, whether this number depends on the event topology, and if additional bricks are extracted in the case a vertex is not found at first.

### Muon Spectrometers

The most downstream section of each supermodule hosts a muon spectrometer. Each spectrometer consists of electronic devices such as drift tubes and RPCs, along with a dipolar magnet. The magnets are 8.75 m wide, 10.0 m tall and 2.64 m in dept; along their yokes for a total of 64 copper spires circulate a 1600 A current, which results in a 1.57 T magnetic field, vertically oriented, in opposite directions in the two arms of the magnet, see Fig. 2.8.

The arms of the magnets consist of 12 iron walls, each 50 mm thick, interleaved with RPCs walls which constitute the active part of the spectrometer. One RPC wall consists of 7 horizontal RPCs triplets. The total number of RPCs in both spectrometers is 924, for a covered surface that exceeds 3000 $m^2$.

Each RPC is made of two 1.1 $\times$ 2.9 $m^2$ high-resistivity ($\rho \sim 10^{11} - 10^{12}\Omega$cm) bakelite slabs, sealed together with a 2 mm gap between them, see Fig. 2.9. The two slabs are kept parallel by means of $\sim$ 300 plastic spacers, glued in their inner sides in a 10 cm lattice configuration. The outer side of the chamber is coated with

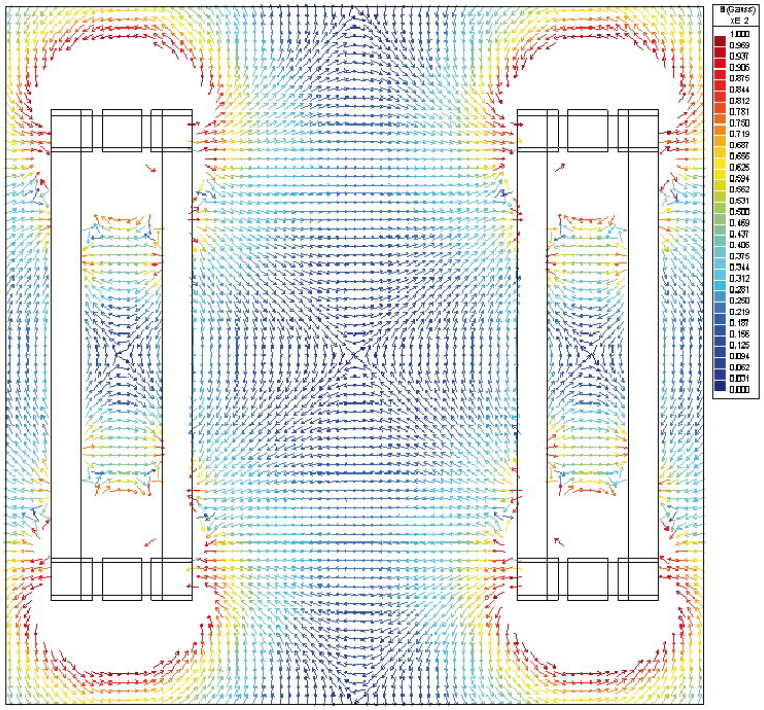

Figure 2.8: Representation of the magnetic field around the two spectrometer magnets.

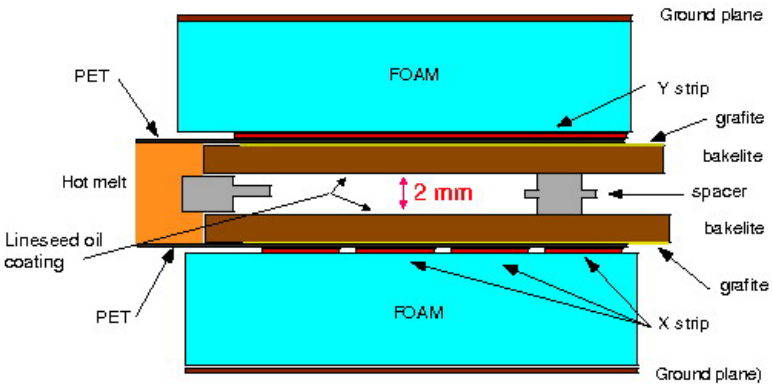


Figure 2.9: Schematic transverse layout of an RPC, sandwiched between the pick-up strip panels.

graphite ($\rho_s \sim 100\text{k}\Omega/\square$)and isolated with 190 $\mu$m thick PET film. The RPCs are flushed with a gas mixture composed by Argon, Freon, Isobutane and $SF_6$ in ratios presented in Tab. 2.2.

| Common name | International code | Formula | Percentage in volume |
|---|---|---|---|
| Argon | | Ar | 75.4% |
| Freon | R134a (ASHRAE [17]) | $C_2H_2F_4$ | 20% |
| Isobutane | R600a (ASHRAE) | $C_4H_{10}$ | 4% |
| Sulfur hexafluoride | 2551-62-4 (CAS [18]) | $SF_6$ | 0.6% |

Table 2.2: The gas mixture used in the OPERA spectrometer.

The RPCs are operated in streamer mode, with a 7.5kV voltage on their electrodes that produce an uniform electric field inside the gas mixture. A ionizing particle passing through the gas produces a high current signal, which is read by induction by two external planes of 2.6 cm pitch copper strips, oriented perpendicularly along the X and Y directions, that give a bi-dimensional reconstruction of the hit position on the detector with a spatial resolution of the order of 1 cm.

Each muon spectrometer is equipped with six planes of Precision Trackers (PT), two upstream, two between the iron arms and two downstream (Figure 2.10). The PTs consist of vertical drift tube planes with an intrinsic resolution of 0.3 mm in the bending direction. Allowing for some misalignment, an overall resolution on each measured coordinate of 0.5 mm is expected. The momentum resolution $\Delta p/p$ is expected to be better than 30% in the relevant kinematical domain.

The Inner Trackers allow a coarse tracking inside the magnet to identify muons and facilitate track matching between the Precision Trackers. They also provide a measurement of the tail of the hadronic energy leaking from the target, and of

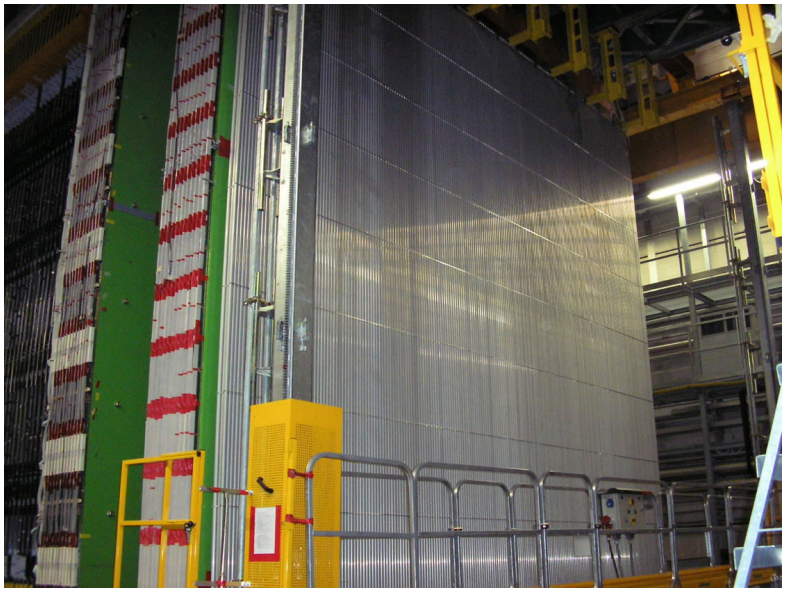

Figure 2.10: View of a precision tracker wall downstream the dipolar magnet of SM2.

the range of muons which stop in the iron. Overall the spectrometers provide the measurements needed for the study of the muonic $\tau$-decay channel and for the suppression of the background from the decay of charmed particles.

### 2.1.3 Data-acquisition, brick extraction, microscope scanning

The electronic detectors provide the trigger for brick extraction, and a probability map on the foregoing brick walls. The brick located in the most probable area is extracted by the BMS.

The candidate bricks are transported in a dedicated area inside the underground laboratories, where the CSs are removed and developed for a prompt analysis in order to confirm/reject the neutrino interaction. If the CSs do not confirm the interaction, the brick is equipped with two new emulsion sheets and placed back in the detector. If the CSs confirm the presence of the interaction, the brick is transported to the outside laboratories and exposed for about 24 hours to cosmic-ray muons. This procedure provides a dense set of passing-through tracks used by the scanning system to locally inter-calibrate the emulsion sheets, and correcting for the spatial misalignment and deformation. The bricks are exposed to the cosmic rays without CSs, allowing to identify which tracks refer to neutrino events and which refer to cosmic-ray muons. Each brick is also exposed to x-ray lateral marking, which will provide a global intercalibration of the emulsion with

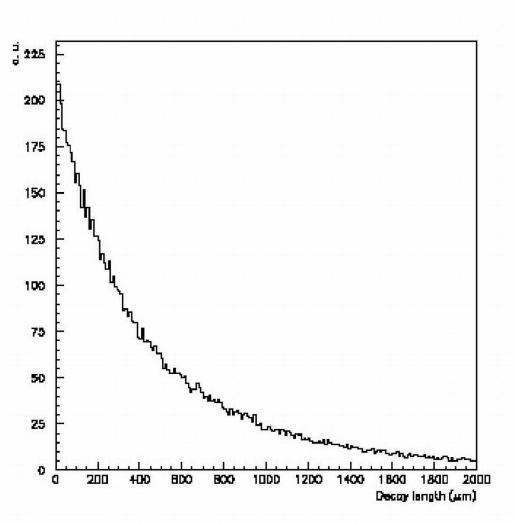


Figure 2.11: $\tau$ lepton decay length distribution, obtained assuming the CNGS energy spectrum and oscillation parameters coming from atmospheric neutrino experiments.

a similar resolution ($\sim 10\mu$m) in a much faster way (few seconds using the x-ray lateral marks, compared to the few minutes, depending on scanned intercalibration surface, using cosmic-ray alignment) once the system will be fully validated.

Subsequently, the brick is disassembled and each emulsion is labelled with an Id number and a set of spots which will provide a reference system during the scanning. Emulsions are developed at LNGS by means of an automatic system, and sent to the scanning laboratories. More about the brick handling and development will be presented in Chapter 3.

## 2.2 Physics performances: $\nu_\mu \rightarrow \nu_\tau$ search

### 2.2.1 $\tau$ detection

The signal of the occurrence of $\nu_\mu \leftrightarrow \nu_\tau$ oscillations is the CC interaction of $\nu_\tau$'s in the detector target ($\nu_\tau N \rightarrow \tau^- X$) through the decay topologies of $\tau^-$ into an electron, a muon or a single charged hadron. The branching ratios (BR) of the three single-prong decay modes are 17.8%, 17.4% and 49.5% for the electronic, muonic and hadronic channel, respectively [20]. For the typical $\tau$ energies expected with the CNGS beam one obtains the decay length distribution shown in Fig. 2.11.

When a $\tau$ is produced in a lead plate it will decay either in the same plate (short decay) or further downstream (long decay), see Fig. 2.12. For long decays, the $\tau$ is detected by measuring the angle between the charged decay daughter and the parent $\tau$ direction. For this measurement the directions of the tracks before

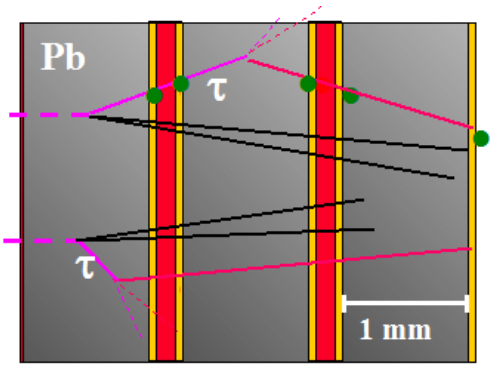


Figure 2.12: Schematic examples of long (upper) and short (lower) decays of $\nu_\tau$ inside the OPERA ECC.

and after the kink are reconstructed (in space) by means of the pair of emulsion films sandwiching the lead plate where the decay vertex occurred. The $\tau$ can also decay in the same lead plate in which the primary interaction occurred or in one of the films or in the plastic base downstream of the vertex plate (short decay). The kink angle is reconstructed, albeit with a lower angular resolution, from the track segments in the emulsion layers on either side of the base. A fraction of the short decays is detectable by measuring a significant impact parameter (IP) of the daughter track with respect to the tracks originating from the primary vertex. The detection of the $\tau$ decay into an electron benefits from the dense ECC structure, which allows electron identification through its showering in the downstream emulsion sheets.

Efficiencies have been calculated for the various categories of $\tau$-decays. They include branching ratios together with losses in brick finding, kink finding, event selection, $\mu$ identification and connection. The total efficiency amounts to 9.1%, an appreciable improvement from the first time, where only long decays of $\tau$ to $\mu$ and electron were considered. Other efficiency improvements are being studied. The inclusion of the $\tau \rightarrow$ 3h decay mode could provide an additional 1.0% to the total efficiency. Another study shows that the brick finding efficiency (BFE) could be increased by 10% with improved analysis and brick extraction strategy[19].

| | DIS long | QE long | DIS short | overall |
|---|---|---|---|---|
| $\tau \rightarrow$e | 2.7 | 2.3 | 1.3 | 3.4 |
| $\tau \rightarrow \mu$ | 2.4 | 2.5 | 0.7 | 2.8 |
| $\tau \rightarrow$h | 2.8 | 3.5 | - | 2.9 |
| total | 8.0 | 8.3 | 1.3 | 9.1 |

Table 2.3: The $\tau$ detection efficiencies in % for the different decay channels of the $\tau$ lepton.

### 2.2.2 Background

The main background sources are charmed decays, hadron re-interactions and large angle $\mu$ scattering.

For the muonic decay mode the presence of the penetrating (often isolated) muon track allows an easier event vertex finding. The potential background from large angle scattering of muons produced in $\nu_\mu$ CC interactions can be reduced to a tolerable level by applying cuts on the kink angle and on the transverse muon momentum at the decay vertex. Possible improved $\pi/\mu$ separation using dE/dx in emulsions would reduce the charm background by 40%[19], see Table 2.4.

Hadronic decay modes have the largest branching ratio but are affected by background due to hadron re-interactions. One of the primary hadrons may interact in the first lead plates and simulate the charged single-prong decay of the $\tau$ . Kinematic cuts are used to reduce this background.

| | $\tau \rightarrow$ e | $\tau \rightarrow \mu$ | $\tau \rightarrow$h | Total |
|---|---|---|---|---|
| Charm decay | .21 | .01 | .16 | .38 (.23) |
| Large angle $\mu$ | | .12 | | .12 (.02) |
| Hadron re-int. | | .09 | .12 | .21 (.21) |
| Total/channel | .21 | .22 | .28 | .71 (.52) |

Table 2.4: Expected number of background events in OPERA in 5 year with nominal beam. Numbers in parentheses correspond to possible background reductions.

| | Signal | | | Background |
|---|---|---|---|---|
| $\Delta m^2(10^{-3}eV^2)$ | 1.9 | 2.4 | 3.0 | |
| OPERA nominal | 6.6 | 10.5 | 16.4 | 0.7 |
| w/ improved eff. | 8.0 | 12.8 | 19.9 | 1.0 |
| w/ BG reduction | ” | ” | ” | 0.8 |

Table 2.5: Expected number of signal and background events in normal, improved efficiency and reduced background conditions.

An important tool for background rejection is the determination of the transverse momentum of the daughter particle with respect to the direction of the $\tau$ track candidate. For $\tau \rightarrow$ e decays the ECC technique is well suited to identify electrons and to determine their energy by measuring the density of track segments associated to the shower in the brick. For charged hadrons and muons, the momentum is deduced from the measurement of the multiple scattering in the lead plates.

The background due to prompt $\nu_\tau$ production in the primary proton target and in the beam dump is negligible. The number of interactions due to these $\nu_\tau$ is

estimated [21] to be $O(10^{-6}) \times N_{CC} \times \epsilon_\tau$, where $N_{CC}$, the total number of $\nu_\mu$ CC events collected, is of the order $O(10^4)$ and the $\tau$ detection efficiency $\epsilon_\tau$ is 10%. The total number of background events in 5 years of data taking is estimated to be 0.71.

# Chapter 3

# Development of OPERA nuclear emulsions

As mentioned in Section 2.1.2, upon completion the OPERA detector will consist of $\sim$ 9 million nuclear emulsions produced by Fuji Co. in Japan. OPERA's target is the largest amount of emulsion ever used in high-energy physics. Emulsion are transported to LNGS by ship and stored in a shielded area in the underground laboratories.

During the neutrino beam exposure electronic detectors will record charged particles produced in neutrino interactions and the event bricks will be identified and extracted by the BMS machine. Every day around 30 bricks will be extracted and their changeable sheets (CS) will be developed underground. CS films will then be scanned with the automated microscopes described in Chapter 4 and, if the track predicted by the electronic detectors is found, the ECC will be brought to the surface laboratories and developed. The daily development capability is around 40$\div$60 bricks (130 CS films underground, $\sim$3,700 films on surface) in five working days per week.

Due to the large number of films that must be daily processed, a fully automated developing procedure has been designed and realized. The whole process has been defined, tested and optimized in order to guarantee large scale quality and stability. Japanese and European groups have carried on the R&D activity regarding OPERA films developing procedure in parallel and there have been also the significant collaboration of Fuji Co. experts.

## 3.1 Emulsion development description

Photographic development is the chemical process by which the latent image stored in the emulsion is made visible by the reduction of silver ions to metallic silver. In *chemical* development, silver ions are provided from the silver halide crystals containing the latent image center. The action of a chemical developer produces a

Figure 3.1: The development room in Lab1 at LNGS. The six development lines are visible together with the set of distribution pipes.

mass of filaments bearing little resemblance to the original crystal. If silver halide solvents, such as sulphite, are present in the chemical developer, some *physical* development may occur, in which silver ions are provided from the solution in the form of a soluble complexes. These compounds are deposited on the latent image center and then reduced to metallic silver. In such a case, the filaments will be shorter and thicker.

Chemical development speed, like many other chemical reactions, depends on temperature: it is faster at higher temperatures while it virtually stops when temperature drops below 10°C[35]. To have homogeneous development on large scale like in OPERA, it is fundamental to keep the processing temperature constant as well as the immersion times. Chemical developers are also dependent on pH, and will maintain the given nominal activity only within a narrow pH range. In general terms, the less alkaline the environment is, the less active the developer will be. Due to this reason the use of an acid stop bath is often recommended at the end of the development to immediately stop the process and have precise control on the effective developing time.

A deeper understanding of the development processes is given by the quantitative methods of electrochemistry[37]. A metal (specifically silver) in contact with a solution of its ions has an attitude to detach electrons, called *electropositivity*, $Ag \rightarrow Ag^{+} + e^{-}$ and its value can be measured by measuring the single-electrode

potential inside the solution. The concentration and activity[1] coefficient of metal ions in solution affects the tendency of the solid metal to dissociate, and consequently it influences the measured potential. The potential difference E is related to the electrode-solution system parameters by the equation:

$$E = E_0 - \left(\frac{RT}{F}\right) \ln \left[ \frac{a_{H^+} (a_M)^{\frac{1}{n}}}{(a_{H_2})^{\frac{1}{n}} (a_{M^{n+}})^{\frac{1}{n}}} \right] \tag{3.1}$$

where $E_0$ is the constant standard electrode potential; $T$ is the absolute temperature; $R$ is the gas constant per mole; $F$ is the Faraday constant; $a_{H^+}$ is the activity of the hydrogen ion; $a_M$ is the activity of the metal; $n$ is the degree of ionization; $a_{H_2}$ is the activity of gaseous hydrogen; and $a_{M^{n+}}$ is the activity of the metal ion. The activity of pure, solid unstrained metal is defined to be equal to 1, as are the activities of hydrogen gas at 1 atm pressure and 1 mole of hydrogen ions per liter.

The loss of electrons by an atom to the surrounding medium is called reduction, while the gain of electrons is called oxidation. When ions in the medium exist in two different states of reduction their relative activities affect the electrode solution potential difference, E :

$$E = E_0 - \frac{RT}{F} \ln \frac{a^{(n-1)+}}{a^{n+}} \tag{3.2}$$

$E_0$ is the potential that exists when the ions are equally active; $a^{(n-1)+}$ and $a^{n+}$ are the relative activities of the ions in the ionized states $(n-1)$ and $n$. At low concentrations the activity is proportional to the concentration itself, thus, in studying oxidation-reduction processes, it is common to write the previous equation in the following way:

$$\Delta E = -\frac{RT}{F} \ln \frac{(\mathrm{OX})}{(\mathrm{RED})} \tag{3.3}$$

where $E$ is called the redox potential. Here (OX) and (RED) are approximately the respective concentrations of the oxidized and reduced forms of the reducing compound. What is of primary importance for our concerns is that development speed is regulated by the magnitude of $\Delta E$.

Several inorganic materials can be used as developers for nuclear emulsions. They can be classified considering their development rate (related to their reduction potential relative to a hydrogen electrode) at fixed pH. The developers generally used for nuclear emulsions are combined chemical and physical developers, sulphite and bromide are solvents of the silver halides. The silver ions in the complex are reduced to metallic silver that precipitates in the gelatin, and plates out on the silver grains. This causes physical development of the latent image grains and also unwanted fog. In order to obtain a successful development, it is

[1] Activity in chemistry is a measure of how different molecules in a non-ideal gas or solution interact with each other. Activity effects are the result of interactions between ions both electrostatic and covalent.

required that the reaction rate of the grains forming the desired image is faster than the development of fog.

As already mentioned, the rate of development, like most chemical reactions, strongly depends on temperature[38]. In the small interval of temperatures ordinary used for development, the relationship between the logarithm of the development time $t$ and solution temperature $T$, is roughly linear:

$$\log t = -KT + Y \tag{3.4}$$

The temperature coefficient $K$ is usually in the $1.55 - 2.02$ range, depending on the photographic materials and the composition of the developer. Furthermore, the potential of pure reducing agents grows linearly with the pH of the solution.

Because of common ion effect, the presence of a soluble bromide in the developing solution lowers the silver ion concentration, and restrains the development rate. This effect generally inhibits the growth of fog more than the development of the latent image. It is particularly important to use bromide in processing nuclear track emulsion otherwise fog will develop in the upper emulsion layers. On the other side an excess of KBr produces a deleterious effect because the silver ion concentration can be driven so low that metallic silver goes into solution destroying the latent image.

The conventional photographic processing steps are:

1. Presoak;
2. Development;
3. Stop;
4. Fixation;
5. Wash;
6. Dry.

In the OPERA experiment, standard procedures need to be modified due to the great thickness of the emulsions in order to have a uniform development and distortion-free emulsions[35]. Furthermore some new steps in the procedure are introduced beside the conventional ones to meet the aforementioned requirements. This is the case of a *Clean* step after the *Stop* bath, to remove residual chemicals, a double *Wash* step, with intermediate water flushing and recycling, and last but not least, a *Drywell* bath with alcohol and glycerin, to avoid drop stains on emulsion surface during the drying.

As an example, the purpose of fixation bath is to remove all the residual silver halide, leaving the metallic silver to form the image. If silver halides are left in the emulsion, they would slowly turn brown and degrade the image. This clearly is an extremely sensitive point in the OPERA perspective, since the emulsions can be

scanned and analyzed in a many months or even years time-span. The most widely used fixing agents are either sodium or ammonium thiosulphate, which form thiosulphate complexes with the silver halide. Silver thiosulphate is soluble in water and it can be removed from the emulsion by washing. It is important to not use an exhausted fixer when processing nuclear emulsion; otherwise some silver halide will remain in the emulsion. After fixation, emulsion must be washed very thoroughly to remove all the silver thiosulphate complexes in the emulsion; any residual would eventually break down, producing silver sulphite which is brown and it would then darken the emulsion. During fixing and washing, emulsions are soft and fragile and can be subject to big distortions, careful handling is therefore necessary. The exposure to distortions during the drying procedure can be mitigated by the use of alcohol-glycerin baths as last step of the whole procedure.

## 3.2 Development facility layout

In order to process the huge amount of emulsions extracted from the OPERA target every day, a dedicated developing facility has been planned, designed and build at the surface laboratories at LNGS[36]. The building, named Lab1, hosts all the activities needed to prepare the emulsions for microscope scanning in all the laboratories of the collaboration:

- cosmic-ray pit for exposure to cosmic rays, needed for intercalibration alignment;
- devices for water demineralization and thermalisation;
- storage tanks for development chemicals;
- chemicals mixing and distribution systems;
- emulsion unpacking and labelling room;
- automated development lines;
- drying and packing room.

The bricks extracted from OPERA after their CS doublet has confirmed the presence of interesting events, are carried from the underground labs to Lab1. They are then exposed to cosmic rays for roughly 24 hours in the *cosmic-ray pit*, which is located around 5 meters underground, and is shielded by a 40-cm-thick iron plate on the ceiling, to stop the soft component of the cosmic flux. The result is an uniform lattice of high-energy muon tracks that pass through the bricks, perpendicularly with respect to the emulsion plates.

The bricks are then brought to the development laboratory, for automatic processing. The laboratory, schematically shown in Fig. 3.3, is located at the first

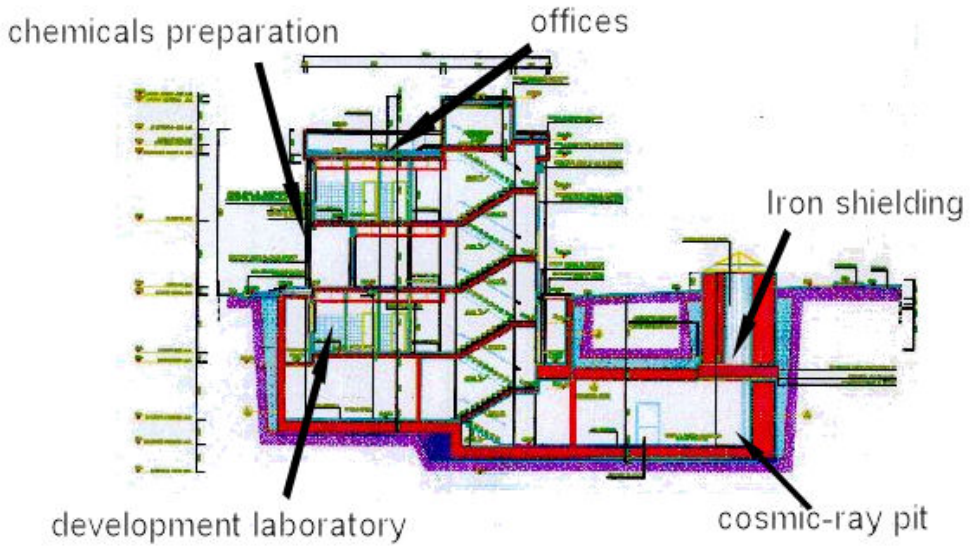


Figure 3.2: Vertical layout of the development facility building (Lab1) at LNGS.

underground floor and is mostly operated in red-light to which the emulsions are insensitive, like in normal photographic rooms. The dark-room part is light-tight thank to an inter-locked double door at entrance side, and a light-trap at exit.

The main parts of the development laboratory are described below:

### Computer room.

Out of the darkroom, the computer room hosts the servers that control the automated machines and the database. The computer room is planned to be connected to the darkroom by means of an *intercom* for easy voice communication of the operators.

### Unpacking room.

In the unpacking room, bricks are dismantled, emulsions are unpiled, labelled and positioned on specifically designed film holders (see Fig. 3.8). A trained group of 3 to 4 operators can fully disassemble a brick in darkroom conditions in less then 15 minutes. The filled-up film holders are then handed to the operator in the development room through a sliding window.

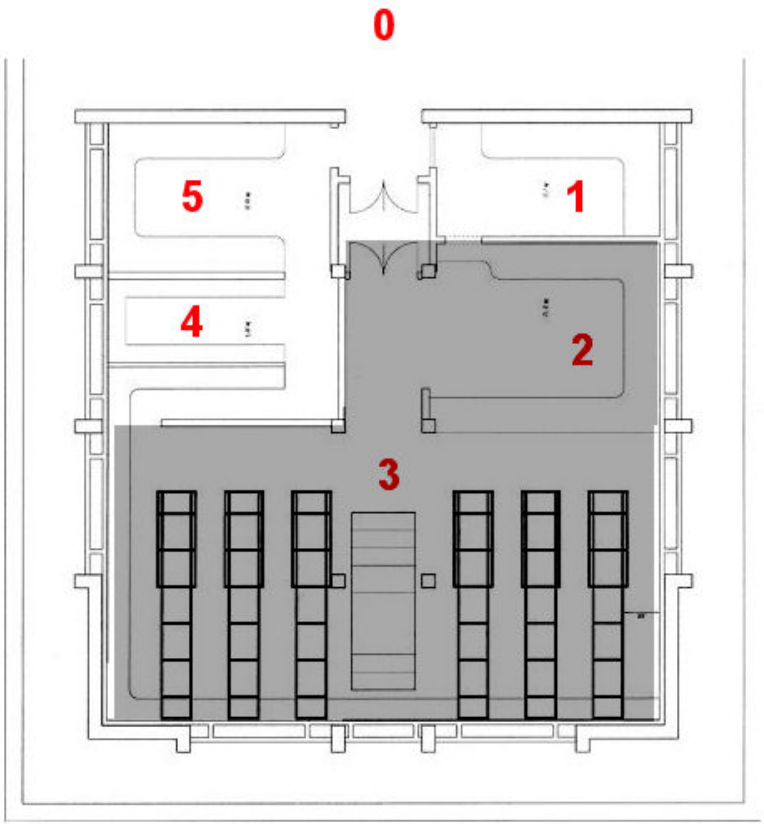


Figure 3.3: Layout of the development room at Lab1. The grayed-out rooms are operated in red-light (Dark-Room). 1) Computer room and control room 2) unpacking and labelling room 3) development lines room 4) drying room 5) packaging room.

Figure 3.4: Photograph of several fully developed emulsion bricks during drying process.

### Development room.

It is the main room where the emulsions are developed. Six automated development lines are installed. At present time, half of them are fully operational and commissioned, the remaining three are under construction. The lines are made of a queue of tanks containing the chemicals and an automated arm which moves the film holders in the tanks according to the immersion times, see Table 3.1. The development lines are described in details in Section 3.4. The developed emulsions are carried to the drying room by means of a conveyor which runs along the walls and collects the film holders.

### Drying room.

The developed films need a slow drying in a temperature and humidity controlled room (see Fig. 3.4), to avoid deformations due to quick drying of emulsion gel. The are stored in this room for up to two days.

### Packaging room.

Once dried, the emulsions can be packaged and sent to the microscope laboratories world-wide for analysis.


Figure 3.5: Two of the buffer tanks for chemicals at ground floor of Lab1.

## 3.3 Chemicals and hydraulic system

This section briefly presents the final steps that has been planned to develop the OPERA emulsions, following several years of darkroom tests, and involved the work of many people inside the experiment. The data are summarized in Table 3.1.

The chemicals needed for the process are prepared at ground floor of the building, where six storage tanks are situated (*Fix1*, *Fix2*, *Glyc*, *Stop*, *Dev*, *Pres*) each of these tanks has a capacity of 1250 liters. These tanks are filled with thermalised (20°C)and demineralized water coming from first underground floor. The chemicals ready for use are then pumped into smaller *buffer* tanks (Fig. 3.5), on the floor right above the development laboratory, see Table 3.2.

The chemicals are then distributed to the development lines through a series of pipes by means of remotely-operated electro-valves. The tanks that contain the solutions are here briefly described:

**Presoak** to allow the developer penetration through the whole emulsion thickness; in the case of OPERA it also help cleaning the emulsion from lead residues, which may contaminate the following chemicals. This usefulness of this step is under investigation, and it might be excluded from normal operation, or reduced to a very short bath.

**Development** is the key process to make the latent image visible, and determines the quality of the emulsion, and its properties such as grain size, fog density,

| Solution | Time | Composition | Volume per liter |
|---|---|---|---|
| Presoak | (10') | Sodium Sulphate<br>Demineralized water | 70g<br>→ 1000 ml |
| Development | 25' | Demineralized water<br>Fuji developer<br>Fuji starter | 750 ml<br>250 ml<br>20 ml |
| Stop | 10' | Acetic acid<br>Demineralized water | 5 ml<br>→ 1000 ml |
| Clean | 10' | Water | 1000 ml |
| Fixation | 35' | Fuji fixer<br>Water | 500 ml<br>500 ml |
| Wash<br>(4 steps) | 4 × 20' | Water | 1000 ml |
| Glycerine<br>+<br>Drywell | 20' | Glycerine (86%)<br>Fuji drywell<br>Water | 235 ml<br>5 ml<br>760 ml |

Table 3.1: OPERA film developing chemical processes with corresponding immersion times and components.

etc...

**Stop** quickly and uniformly halts the developing process throughout the emulsion.

**Clean** washes away the chemicals residues from the films. This intermediate step has been introduced to avoid contamination of solutions along the line in order to prolong the lifetime of the solutions themselves.

**Fix** frees the emulsion from the residual silver, giving to the emulsion its final aspect.

**Wash1** cleans the emulsion from all the chemicals and residues of the treatment. It is made of two 20-minute-long baths, with water that has been collected from following tank and recycled.

**Wash2** is analogue to Wash1 tank, with two consecutive baths, but is filled with clean fresh water (not demineralized).

**Drywell** is a mixture of glycerine, water and Fuji Drywell, used to thicken the emulsions, reduces the deformations and avoids drop stains on the film surface during the drying period.

The exhaustion of all these chemicals is done in underground tanks situated out of the main building. Some of the solutions are mixed together in the tanks, others are stored separately. The tanks are periodically emptied by authorized firms for appropriate treatment and wasting.The foreseen volume of exhaustion is 6 $m^3$/week for *Development*, *Stop*, *Glycerine* and *Drywell* solutions, 3 $m^3$/week for *Fixation*, about $30m^3$/week for water.

| Name | Capacity (liters) | Kind of water used |
|---|---|---|
| Presoak | 500 | Demineralized |
| Development | 250 | Demineralized |
| Stop | 250 | Demineralized |
| Clean and Wash2 | 500 | Fresh water |
| Fix | 750 | Demineralized |
| Wash1 | 500 | Recycled from Wash2 |
| Glycerine | 250 | Demineralized |

Table 3.2: Description of the buffer tanks used to store chemicals used for the development process.

## 3.4 Development line

This section describes in deeper details the automated development lines hosted in the first underground floor of Lab1[2].

The goal of the automated lines is to develop the high number of emulsions needed for the OPERA experiment, providing high and uniform quality films to the scanning laboratories worldwide. The full development process of each brick lasts about 3 hours and a half; this conveys the impossibility to develop the bricks one by one, therefore the development lines must be able to handle up to 5 bricks simultaneously on each line, with the mechanical arm serving each process at the right time, granted that the temperature conditions are always stable.

### 3.4.1 Hardware description

The mechanical structure of the lines layout out in Fig. 3.6 is made of aluminum rods, standing on concrete bases. These bases are build on top of the tiled waterproof floor, while the operators can walk on a grate floor, elevated by ∼20 cm. The lines are approximately 4.5 meters long, 80 cm wide and 1.2 m high, each one equipped with 8 inox steel tanks, 5 of which have a capacity of 30 liters, the remaining 3 have a capacity of 45 liters.

A mechanical arm (Fig. 3.8), mounted on an aluminum bridge, can slide horizontally forth and back for the whole length of the line. The arm can slide vertically along the bridge and is equipped with a jaw which allows to carry the film holders containing the emulsions and deposit them into the tanks. The vertical and horizontal movements are actuated by 2 Sanyo Denki step-motors, controlled by two

[2]The mechanical design is due to Elio Buccheri and Alessandro Pelosi of "La Sapienza" University of Rome, the low-level hardware implementation has been designed by Elio Buccheri, while the high-level control software has been designed and coded by Enrico Carrara. The whole project has been directed under the responsibility of Prof. Giovanni Rosa of "La Sapienza".

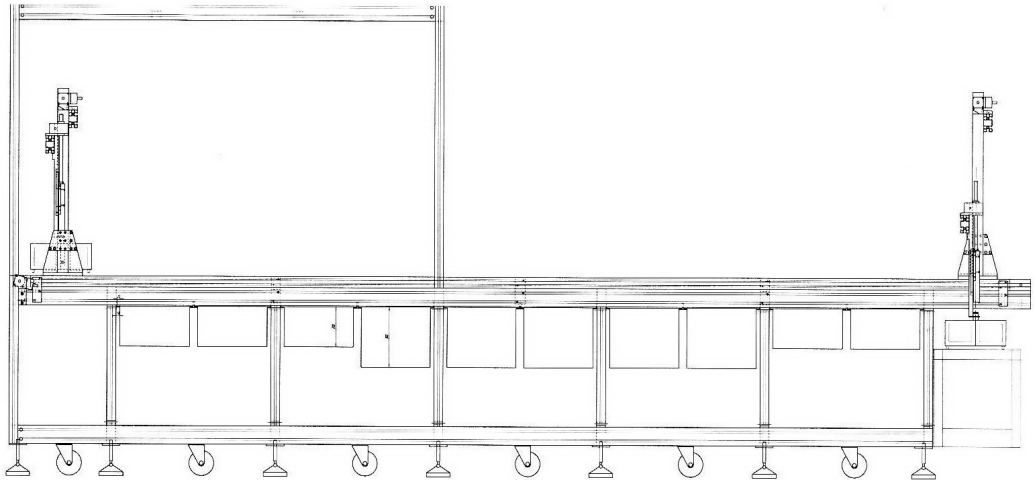

Figure 3.6: Schematic layout of development line from side view.

RTA Mind-S motor drivers. The logics of the movements are directed by a Crouzet Millennium 2 PLCs (*Programmable Logic Controller*), which receive information about the status of the machine from several magnetic induction sensors.

Furthermore, each tank is equipped with a Siemens LOGO PLC (see Fig. 3.9) which performs the following operations:

- keep track of the immersion time of the brick in the solution;
- count how many cycles the current solution has been used for;
- control the inlet and outlet electrovalves;
- control the solution level by reading an infrared depth sensor;
- comunicate with the remote PC.

Unlike general-purpose computers, the PLC is designed for multiple inputs and output arrangements, extended temperature ranges, immunity to electrical noise, and resistance to vibration and impact. Programs to control machine operation are typically stored in battery-backed or non-volatile memory. A PLC is an example of a real time system since output results must be produced in response to input conditions within a bounded time, otherwise unintended operation will result. This makes it well suitable for the use in the OPERA development laboratory.

The tanks are connected to buffer tanks containing the chemicals and situated on the upper floor by a distribution system of several pipes, controlled by the aforementioned electrovalves. The exit pipes collect the liquids to the exhaustion tanks.

The starting position of the development line is the so-called *Home* position, where the operator places the film holder to be processed. At the further end of the

Figure 3.7: Photograph of the first development line.

development line, running around the wall of the room, a conveyor belt collects the film holders and, completed the development process, carries them to the drying room through the light trap. Therefore the bridge can move horizontally on 10 different positions, the 8 tanks plus the home and conveyor position. Each position is marked by a metallic plate, which, by means of the magnetic inductive sensors, indicates the stopping point for the horizontal movement of the bridge. Additional 4 metallic plates represent, in binary code, the progressive number of the position, allowing the control program to know at which tank the bridge is standing.

The machines are connected by cables to racks that are hosted in a closet in the unpacking room, such racks contain the higher level logics of the machines and power-supplies, which cannot be in the development room due to security reasons, mainly for the presence of liquids. The racks offer an interface to the remote control computer through a collection of *Field Point* modules.

Field Points are designed for measurement, industrial control, and data logging applications that require reliable, rugged systems involving diverse sensors and actuators located centrally or spread over large distances. Field Points includes networking capabilities for distributed I/O via an ordinary Ethernet network cable. A full system can be built up by adding dependable I/O modules and communication interfaces. The modules used are commercial National Instruments modules; more specifically, each rack has a FP-1601 Ethernet Network Interface, to which 1 analog input module, 2 digital output modules and 4 digital input modules. Their characteristics are summarized in Tables 3.3 and 3.4.

The Field Points are then connected with an Ethernet cable to the control PC, which runs the scheduling program, that automatically executes the full develop-

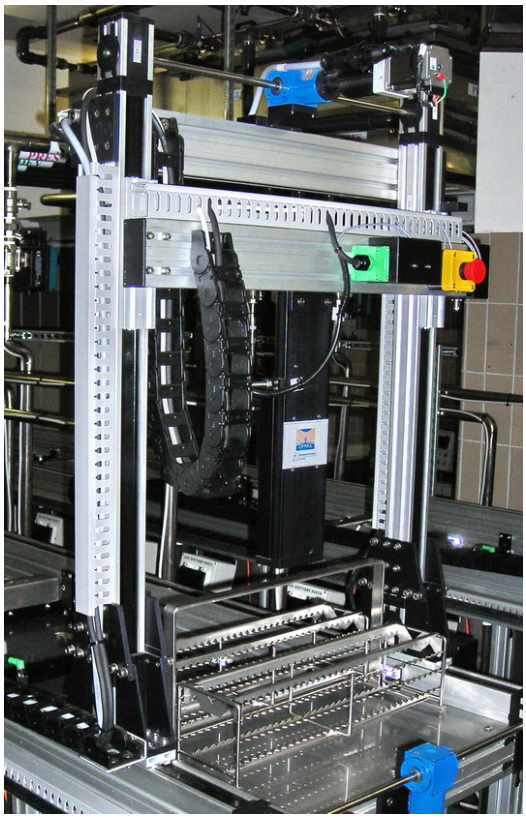

Figure 3.8: Photograph of the mechanical arm with an empty film holder at *Home* position.

| Module name | Type | Main characteristics |
|---|---|---|
| NI FP-1601 | Ethernet Interface | TCP/IP<br>100BaseTX (100 Mb/s)<br>10BaseTX (10 Mb/s) |
| NI FP-DI-301 | Digital Input | 16-Channel / 24 VDC |
| NI FP-AI-112 | Analog Input | 16-Ch/16 bit Voltage |
| NI FP-DO-401 | Digital Output | 16-Ch/ 5-30VDC-2A |

Table 3.3: Characteristics of the Field Point modules used.

| | |
|---|---|
| Dimensions | $10.7 \times 10.9 \times 9.1$ cm$^3$ |
| Weight | $\sim$130 g |
| Operating temperature | -40 to 70°C |
| Storage temperature | -55 to 85°C |
| Relative humidity | 10% to 90%, noncondensing |

Table 3.4: Specifications common to all the Field Point modules.


Figure 3.9: Photograph of PLCs controlling the tanks of one development line.

ment procedure, without the operator intervention.

### 3.4.2 Software description

The high-level software that controls the development lines runs under Microsoft Windows© on a Personal Computer in the computer room. A single computer can host one program instance for each of the six development lines, but for redundancy matters, it is planned to have just one instance of the program running on one PC. The program has been written in the `.NET` framework, using the `C#` programming language. This choice follows from the power and ease of use of the language, which is a strongly-typed object-oriented programming language. The obtained code is easy to manage, re-use and is easily readable by any programmer familiar with the wide-spread `C++` language. Object-oriented programming (OOP) offers a high level of abstraction of the code, which allows a safe encapsulation of software functionalities in well-defined portions of the code, making the whole structure of the program solid and reliable. Among the other benefits of OOP in writing the program for the development machine is the possibility to use the design patterns[3] [34].

The control software relies on middle-ware component, provided by National

[3]The term *design patterns* refers to any general, repeatable solution to a commonly occurring problem in software design. Some of these commonly occurring problems have implications and solutions particular to object-oriented development.

Instruments, which is a OPC (OLE for Process Control, where OLE stands for Object-Linking and Embedding) server, to communicate seamlessly with the Field Points. The program is internally structured in different layers, which are independent from each-other. A first low-level layer corresponds to a library, which provides only the basic functionalities of the machine, analog to the manual operation, for example the *atomic* action "drop the film holder in the tank" (see Fig. 3.10). A second layer provides a set of mid-level functionalities, which requires the interaction of both input and output signals from the PLCs. An example of such functionalities is the "move the films to the next tank" action, which is made of the following atomic actions: move to the selected tank, grab the film holder, move to the following tank, drop the film holder. The third layer of the program is the *scheduler*, which provides the high-level functions that allow to manage an arbitrary number of bricks on the same line, taking care of the correct immersion times, or resolving the race conditions of more than 1 brick that require the intervention of the mechanical arm.

Two additional layers can be included in the picture: the *Graphical User Interface* (GUI), which allows the interaction of the user with the scheduling program, and the Data-logging layer, that stores information about the machine operations on virtually any media, file system, database, network resource, etc.

### The OPC Server

OPC is the original name for an open standards specification developed in 1996 by an industrial automation industry task force. The standard specifies the communication of real-time plant data between control devices from different manufacturers. OPC was designed to bridge Windows based applications and process control hardware and software applications. It is an open standard that permits a consistent method of accessing field data from plant floor devices. This method remains the same regardless of the type and source of data.

OPC servers provide a method for many different software packages to access data from a process control device, such as a PLCs or DCS[4]. Traditionally, any time a package needed access to data from a device, a custom interface, or driver, had to be written. The purpose of OPC is to define a common interface (see Fig. 3.11) that is written once and then reused by any business, SCADA[5], HMI[6], or custom software packages. Once an OPC server is written for a particular device, it can be reused by any application that is able to act as an OPC client. OPC servers use Microsoft's OLE technology (also known as the Component Object Model, or COM) to communicate with clients. COM technology permits a standard for real-

[4] *Digital Communication System.*

[5] *Supervisory Control And Data Acquisition*, refers to a large-scale, distributed measurement and control system.

[6] *Human Machine Interface* is the aggregate of means by which the users interact with a particular machine, device, computer program or other complex tool.

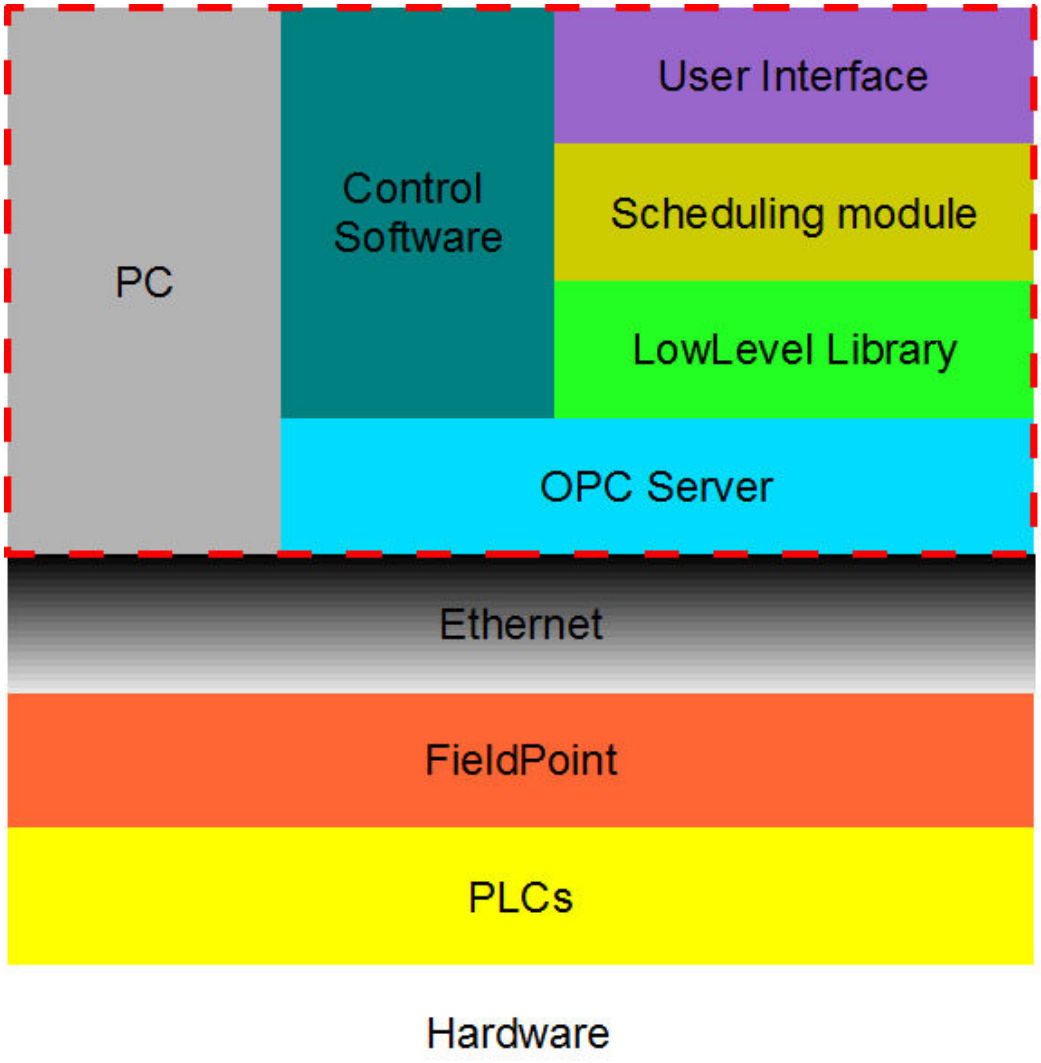


Figure 3.10: Layout of hardware and software infrastructure. The bottom half is the hardware implementation, while the top half enclosed in a red border is the software running on the control PC.

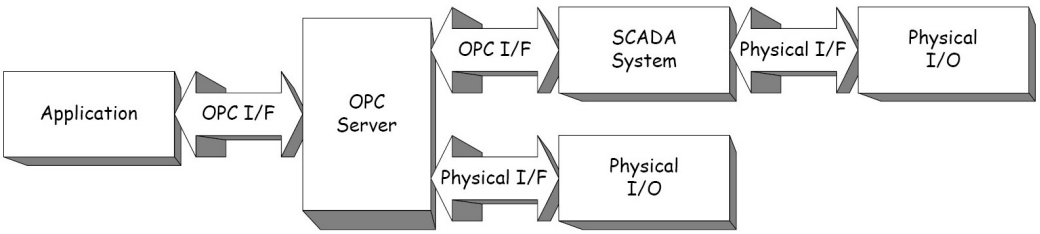


Figure 3.11: Layout of the OPC Server/Client relationship.

time information exchange between software applications and process hardware to be defined.

The choice to use the OPC standard follows from the long-life of the OPERA experiment, compared to the fast-progressing industry of automation technologies. In the case of a hardware upgrade, or hardware failure with consequent installation of a different model or different manufacturer, the change would just require a different OPC server implementation, leaving the rest of the software completely untouched.

### Low-level library

The low-level library is a collection of *classes*[7] written in `C#` that provides a direct interface to the available hardware. The architecture of the library has been designed to conform as much as possible to the real hardware components, for easier identification of the *objects* and their functionalities.

The first class is the `FieldPoint` class, which is made of several instances of the `Module` class, each of which contains several instances of classes derived from the `Chanel` *abstract class*[8]. The `FieldPoint` class exposes only few basic *methods*, such as channel reading and writing and read/write of the configuration file that stores all the mapping of real modules and channel connections. Such `FieldPoint.cfg` file is in XML format. The `FieldPoint` object creates and abstraction layer on the physical channels, allowing the rest of the software to refer to the channels by their actual use instead of their physical position. In other words, for example, if the digital signal of the film holder present at *Home* position reaches channel 6 of module 3 of a given Field Point, the `FieldPoint` object maps it into the `ChannelTypes.CratePresentHome` enumerator; so the rest of the program simply has to call on the mentioned enumerator instead of the actual physical position of the signal.

The second layer of functionality is give by the `DevLine` class, which contains an instance of `FieldPoint`, several instances of classed derived by the `Position` class,

[7] In object-oriented programming, a class is a programming language construct used to group related fields and methods.

[8] An abstract class is a class that cannot be instantiated and is designed only as a parent class from which child classes may be derived.

more precisely the 8 different `Tanks`, the `Home` and `Tapis` positions. Last member of the `DevLine` class is the `Arm` class, which represents the mechanical arm of the line and takes care of the various signals that come form the `FieldPoint`, allowing the atomic actions of the machine. The `Arm` exposes, through `DevLine`, the methods corresponding to the manual operation of the line, such as *MoveForward()*, *MoveBackward()*, *GetCrate()* and *DropCrate()*. Furthermore, `DevLine` also exposes the methods that control the tanks of liquids, for example *DevelopFlush* or *DevelopRefill* and so on.

### 3.4.3 Task Scheduling

The third layer is implemented in another library, called `DevSched` that collects the classes used for the scheduling of the development processes. The basic element is the `DevTask`, which is just the foreseen action that the mechanical arm needs to perform, such as moving the film holder from tank A to tank B.

The tank PLCs are set so that they will send a signal to the PC when there are 5 minutes remaining on the immersion time of the current brick. At this point a `DevTask` object will be inserted in the `Schedule` object by the `Scheduler` object. The former is just a time-ordered collection of `DevTasks`, while the second is a manager, that places the tasks in the queue, and eventually reorders them if there are race conditions, such as two overlapping operations. At elapsing of the 5 minutes timer, the `Scheduler` invokes the `TaskExecutor` which unwraps the information of the `DevTask` and sends the appropriate commands to the `DevLine` of the low-level library.

The described architecture might seem overcrowded with interacting objects, but is required in order to provide safe and reliable executions of the tasks in any operation conditions. In facts the above layout is capable of handling an arbitrary number of bricks on any number of tanks, for any immersion times and eventual failures that bring to delays. Such a flexible scheduling is needed to prevent loss of quality in developing emulsions due to unforseen problems with the line or operator activities, i.e. the bricks can be positioned at the *Home* position after unpacking at any time, without altering the global scheduling of the machine.

### 3.4.4 Data logging

An interesting use of design patterns is in the data-logging functionality of the program. The requirement for flexibility needs the program to in principle be ready for logging its operations on any kind of media, file or any kind of database. The result is obtained using the subscriber pattern.

In such patter, the source of the information to be logged, in our case the developing line, implements the `ISubscriber` interface, while the target on which the data should be logged implement the `IObserver` inferface. The former interface includes the *Subscribe()*, *Unsubscribe()* and *Notify()* methods, while the latter only

include the *Update()* method.

The source object has a list of its subscribers, object that called its *Subscribe()* method, waiting for information to be delivered. When such information is needed to be logged, the source object stores it into a standardized `Message` object, and invokes its own *Notify()* method. This method iterates through the list of subscriber objects, invoking their *Update()* methods and passing them the `Message` instance.

It is now up to the subscriber implementation to take the `Message` object, extract the data from it, and log it on the chosen medium. This completely frees the programmer of the source object from any knowledge of the kind of targets that will need its data.

At present time the interfaces are ready on the control program, and an Oracle subscriber object is being developed by Alessandro Ruggeri of "La Sapienza", implementing the `IObserver` interface.

# Chapter 4

# The OPERA microscope in Padova

## 4.1 Introduction

The photographic emulsion technique has been used in particle physics for decades; however, since the beginning, it required a tremendous effort in terms of time and manpower, in order to manually inspect and analyze the films. Due to this limitation only small experiments could afford the use of ECC.

The integration between microscopes and new computer-based technologies recently allowed to use this technique also in massive target experiments. The emulsion automated scanning was pioneered by the group of Nagoya University (Japan). The first application of an automatic system, called *Track Selector* (TS), was used for the DONUT and CHORUS experiments [26, 27]. Later versions before OPERA times, reached the speed of $\sim 2$ cm$^2/h$, in the *Ultra Track Selector* (UTS).

The OPERA experiment requires an improvement of about a factor of ten in speed compared to DONUT or CHORUS, i.e. a speed of about 20 cm$^2/h$. To achieve this goal, two different *R&D* programs were carried out, a Japanese one at Nagoya University, a second one in different European institutes.

The Nagoya University group aimed to a further improvement of the UTS system (the so-called Super-UTS). The key features of the S-UTS are the high speed camera with 3 kHz frame rate and a piezo-controlled displacement of the objective-lens, synchronized to a continuous stage motion in order to avoid "go-stop" of the microscope stage while taking images. The system uses Fast Programmable Gate Arrays (FPGAs), fast memory and a grabber board connected to the CCD camera ($512 \times 512$ pixel resolution).

The European groups followed a different approach, initiated by the Salerno group with the SySal system for the CHORUS experiment [28], the so-called *European Scanning System* (ESS).

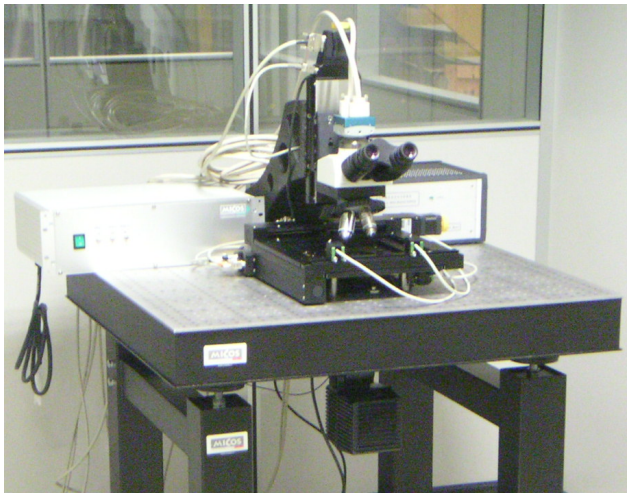

Figure 4.1: Picture of the OPERA microscope in Padova right after installation.

The philosophy of this project is that using the state-of-the-art commercial hardware and software components, conceived in a modular structure, it is possible to achieve the flexibility needed to upgrade the system following the constant technological progress in the computer and microelectronics world.

The Padova group joined the European Scanning project for the OPERA experiment with the installation and operation of an automated microscope in early 2007 (Fig. 4.1).

## 4.2 Scanning system layout

The main components of the ESS microscope are (Fig. 4.2):

- a support optical table holding the components in a fixed position;
- a motor driven scanning stage for horizontal (XY) motion;
- a granite arm which acts as an optical stand;
- a motor driven stage mounted vertically (Z) on the granite arm for focusing;
- optics;
- digital camera for image grabbing mounted on the vertical stage and connected with a vision processor;
- an illumination system located below the scanning table;
- a PC with a high-performance acquisition card installed.

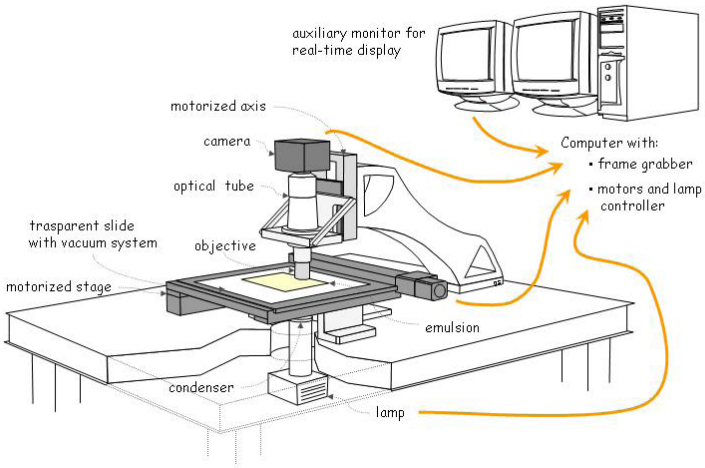


Figure 4.2: Layout of the standard European Scanning System.

The photographic emulsion is placed on the glass plate and kept still and flat by means of a vacuum system. During the scanning, the optical system is moved vertically, with the focal plane spanning through the whole 44 $\mu$m thickness of the emulsion. Up to fifteen equally spaced tomographic images of each field of view are grabbed by the CCD camera with a 8-bit precision (resulting in 256 gray levels palette).

Images are then acquired and processed by the board hosted in the control workstation. Several filters are applied to improve the image. Often the image of the emulsion is not very clear due to shadows caused by grains that are not in the focus plane or to scratches and dirt. Hence a convolution filter is use to enhance the contrast between focused grains and background, while the image is reduced to 1 bit color depth using a well-chosen threshold. The resulting black&white image is analyzed with clustering procedures, where each cluster (groups of dark pixels of given shape and size) represents a grain in the emulsion. Grains may belong to tracks of passing-through particles, or be *fog* grains. Fog is made of single random darkened grains and is the emulsion equivalent of noise in electronic devices.

The following step consists in combining grains from different layers to recognize geometrical alignments. A sequence of aligned grain is called a *micro-track* and is geometrically reproduced as a segment, see Fig. 4.3. The tracking efficiency can be affected by distortions of the track, which may occur due to the development process. The correction algorithm relies on a calculated local distortion vector, with some basic assumptions (e.g. the point at the interface between the emulsion and the plastic base remains in its original position[25], see Fig. 4.4). Micro-tracks on the top and bottom emulsion layers are connected across the plastic base to form a *base-track*. The particle track position and slope is determined

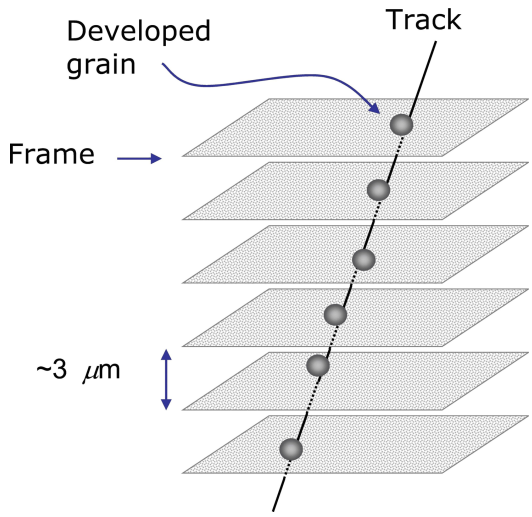


Figure 4.3: The micro-track finding algorithm, searching for aligned grains in different emulsion layers.

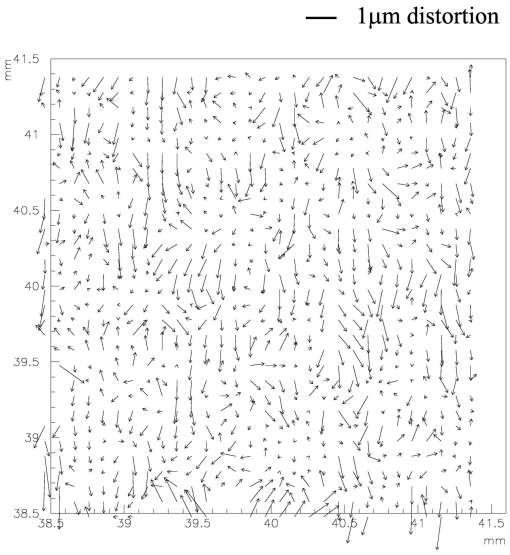


Figure 4.4: Measurement of the emulsion distortion at the centre of an emulsion film (from the OPERA proposal). The scanning area is $\sim$ 3 mm $\times$ 3 mm. The vectors indicate the distortion direction. The absolute value of the distortion is indicated by the length of the arrow.

by a linear fit of base-tracks through the emulsions [29], see Fig. 4.5.

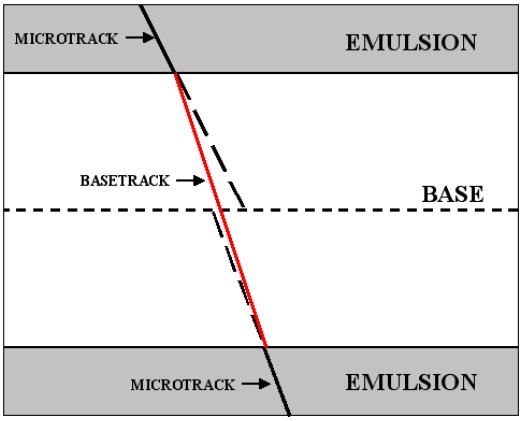


Figure 4.5: The principle of base-track reconstruction: the micro-tracks matching is obtained when an acceptable agreement in slope and position is found. The base-track is formed by joining the two points closer to the base.

## 4.3 Mechanical stage

### 4.3.1 Horizontal stage

The scanning table and the vertical stage have been developed in collaboration with the Micos company by modifying commercial products; they are equipped with stepping motors "Vexta NanoStep RFK Series 5-Phase Microstepping System" produced by the Oriental Motor company. The motors are driven by a 4-axis "FlexMotion PCI-7344" board provided by National Instruments and inserted into the host PC.

The ESS uses a Micos "MS-8" scanning table with 20.5 cm range in both horizontal directions. The coordinates are read out by two linear encoders with a resolution of 0.1 $\mu$m. External optical limit switches are mounted on each axis and manually set.

The motion of the horizontal stage (maximum speed, acceleration, deceleration, ...) was set in order to minimize the time which is needed to move from one field of view (typically $\sim$350 $\mu$m wide) to the next one.

### 4.3.2 Vertical stage

The vertical stage is the Micos LS-110 model. It is equipped with a linear encoder (resolution 0.05$\mu$m) and limit switches. During data taking, the vertical stage moves at constant speed calculated by taking into account the camera frame rate, the number of desired frames and the emulsion thickness (44 $\mu$m). With a frame rate of about 400 frames/s and 15 levels per emulsion layer, each image is acquired at a vertical distance of about 3 $\mu$m; the resulting speed is about 1150 m/s; the

time needed to scan an emulsion layer is about 55 ms (including the time for acceleration, deceleration and synchronization with the host).

## 4.4 Optical system

Great efforts in the OPERA scanning program are devoted to the optical design and set-up. It consists of light source, diaphragms, light condenser, high-quality 50x objective and CCD camera. All these components must be perfectly aligned and tuned in order for the resulting image to have the maximum contrast, smallest aberrations and deformations. A brief description on each component follows, from top to bottom in the actual set-up.

### 4.4.1 CCD camera

The goal of 20 $cm^2/h$ scanning speed requires a frame acquisition time $< 4$ ms and megapixel resolutions. The ESS is equipped with a Mikrotron MC1310 high-speed megapixel CMOS camera with Full Camera Link interface. Its image sensor is the Micron MT9M413 which delivers up to 10-bit monochrome 1280 $\times$ 1024 images at over 500 frames per second. The sensor size is 20 mm (along the diagonal) and its pixels are 12 $\times$ 12 $\mu m^2$ large.

### 4.4.2 Objective

It is one of the key elements of the whole apparatus. The objective must be accurately chosen, taking into account the following considerations and design requests. Since the order of magnitude of the pixel size of the mentioned megapixel camera is $\sim$10 $\mu$m and the size of processed grains in the emulsion is about 0.8 $\mu$m, in order to have a resolution of a few pixels for each grain, the total *Linear Magnification* of the image should range from 40:1 to 60:1 (corresponding to about 3.2 and 4.8 px/grain respectively).

In order to scan the full depth of the emulsion, the *Working Distance* (WD) of the objective must be at least 300$\mu$m, moreover the *Numerical Aperture* (NA) should be as large as possible. The requirement for an objective that reads an OPERA emulsion is NA >0.8 since a sub-micron resolution is needed. It has to be taken into account that the spherical aberration[1] increases as the third power of the NA. To avoid this unwanted effect, the *oil-immersion objective* is used, since typical immersion oils have a refractive index of 1.51; therefore light rays passing through the emulsion sheet encounter a quite optically homogeneous medium because the refractive indexes of the emulsion and plastic base are respectively: $n_{emulsion} = 1.51 \div 1.52$ and $n_{base} = 1.48$; this is referred to as *Homogeneous Immersion* (HI)[30].

[1] More precisely the *transverse* component of the spherical aberration.


Figure 4.6: Close up photograph of the used objective, mounted on the objective holder designed and developed in Padova.

Another important parameter is the *Depth of Field* (DOF), which is the axial range through which an objective can be focused without any appreciable change in the image sharpness. This parameter depends on other design values according to the following formula:

$$\mathrm{DOF} = \frac{n\lambda}{\mathrm{NA}^2} \tag{4.1}$$

, where $\lambda$ is the light's wavelength (in our system the mean value of $\lambda = 550$nm can be used); it should be tuned to allow for the tomographic scanning of the emulsion, avoiding to have grains from different layers which appear on focus in the same image. For our needs, a value of DOP $< 3\mu$m is suitable.

The last crucial point is the *Resolution* (R), that is defined as the smallest distance between two points on a specimen that can still be distinguished as two separate entities. It is expressed by the formula R $= 0.61\lambda/\mathrm{NA}$. The resolution for our microscope apparatus should be less than 1 $\mu$m. The chosen objective (see Fig. 4.6) is a Nikon CFI Plan Achromat 50x oil, NA 0.90, WD 0.35 mm, $f_{obj} = 4$ mm objective, which must be used in *infinity-corrected systems* (ICS). The objective is designed so that light emerging from the rear aperture is focused to infinity, and a second lens, known as *tube lens*, forms the image at its focal plane ($f_{\text{tube lens}} = 200$ mm).

### 4.4.3 Condenser

Correct adjustment of the substage condenser consents to take full advantage of the resolving power of the whole optical system. This is the case when the numerical aperture of the condenser is (almost) equal to the one of the objective and the *Köhler illumination*[30] is realized[2]. The choice of the used condenser has been affected by the requirements on the working distance (at least 5.3 mm) and by the commercial offers. The only available condenser with a sufficient WD is a Nikon Achromatic Condenser, with only NA = 0.65. This value is considerably smaller than 0.90, thus providing a non-optimal performance for the used objective.

### 4.4.4 Illumination system

Due to the low numerical aperture of the condenser mentioned in the previous section, setup of the illumination has to be exploited at its best:

- the iris diaphragm incorporated below the condenser is completely open;
- the focus of the condenser is put in the emulsion plane with high accuracy;
- a diffusive filter (frosted glass) is located below the condenser, to provide a more homogeneous illumination entering the condenser, minimizing the effects of spherical aberration (the used condenser is not aplanatic).

The requirements for the light source are simpler than the previous ones since a diffuser is used: only brightness needs to be adjusted for the diffuser to homogeneously illuminate the field of view. It avoid also a fine adjustment of the position, inclination, and so on. We are using the Schott KL2500LCD light source (see Fig. 4.7), a tungsten halogen lamp with a computer controlled power supply, with a 10 mm diameter fiber optics located 200 mm below the condenser.

## 4.5 Acquisition infrastructure

### 4.5.1 Acquisition Software

The online DAQ software for the emulsion automatic scanning and track segments reconstruction was developed in the object-oriented C++ language. It is based on a modular structure where each object carries out a well defined task. Selecting

[2]The Köhler illumination technique is recommended by all manufacturers because it can produce specimen illumination that is uniform and free from glare, thus allowing the user to realize the microscope's full potential. The condenser is adjusted in order to project in the best focal plane of the objective an image of the field-diaphragm. When the condenser is not in focus, due for examples to mechanical limits, only a fraction (the paraxial) of the emerging ray light can enter the objective front lens and realized numerical aperture decreases.

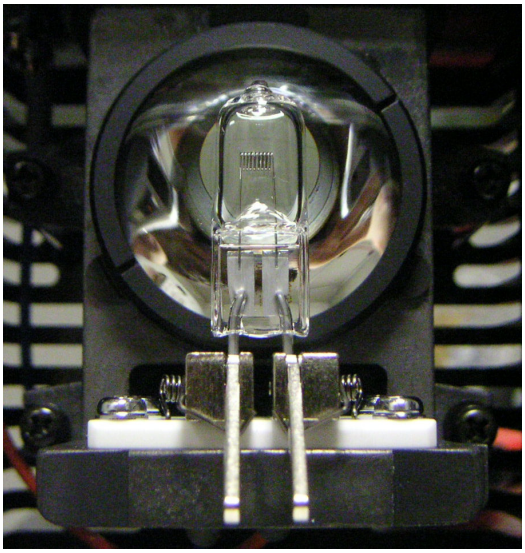

Figure 4.7: Close up photograph of the halogen lamp of the illumination system.

the object and opening the configuration window is possible to insert parameters in order to configure each step of the acquisition process. In Fig. 4.8 the program control panel and the parameter window of the main object are shown.

The list of all modules with their functionality is given in Tab. 4.1.

| Name of the module | Functionality |
|---|---|
| Objective | stores the information relative to the used objective and performs the pixel to micron conversion |
| Odyssey | drives the Odyssey board |
| FlexStage | is interfaced to the stage controllers and sets the movement modalities |
| SmartTracker | is responsible for track pattern recognition, recognizing sequences of geometrically aligned clusters. |
| SmartFitter | performs the track fit. |
| DataIO | handles data Input/Output. |
| SheetMap | transforms coordinates and vectors from the current stage reference frame to the emulsion local reference system defined by a grid of fiducial marks printed on the emulsions). |
| VertigoScan | is the steering module, which uses all the other objects to control the scanning. |

Table 4.1: List of modules composing the on-line acquisition software.

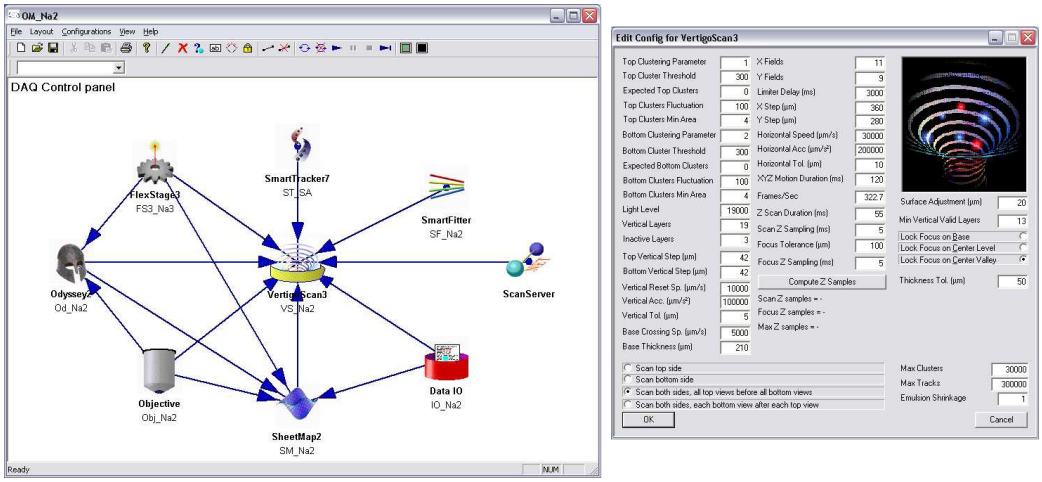


Figure 4.8: Left: the control panel of the ESS online DAQ, where the objects with their configuration files are represented. Right: the window for parameter setting of the main object configuration.

The scanning output is a collection of raw data files (in binary format) which are saved either on filesystem, or on an Oracle Data Base. The high-level operations such as *Scan-Back*[3] of the tracks through the brick are database-driven.

### 4.5.2 Acquisition hardware

The frame grabber and the image processor are integrated in the same board, a Matrox Odyssey Xpro, specifically designed to perform on-board image processing. The on-board processor is a Motorola G4 PowerPC supported by a Matrox custom parallel processor specifically designed to quickly perform local and point-to-point operations. It is equipped with a 1 GB DDR SDRAM memory; the internal I/O bandwidth can achieve over 4 GB per second transfer rate, while the external rate reaches 1 GB per second. A Full Camera Link connection allows an acquisition rate from the camera of up to 680 MB/s.

At present, a camera frame rate of 377 fps and 8-bit gray level images are used, corresponding to an acquisition rate of 471 MB/s. By acquiring 15 frames per 44 $\mu$m emulsion layer, an acquisition time of $\sim$40 ms is used for each field of view. Typical values are a synchronization time of 15 ms, a mean time of $\sim$ 90 ms for the field of view change, a field of view of about 400 $\times$ 300 $\mu$m$^2$ and a superposition between contiguous fields of 30 $\mu$m[31].

Once grabbed, each image is analyzed using image processing techniques like filters, binarization and clustering (for more details see [29]); the grains are recognized as clusters of black pixels. The number of clusters available for tracking

[3]See Chapter 5.

depends on the threshold and on the selection cuts in the cluster area.

## 4.6 Offline analysis

The positions and angles of the detected tracks, for each emulsion layer, are recorded as micro-tracks and are connected off-line to form base-tracks, whose positions and angles are not affected by distortions. After base-tracks in a series of emulsion films are collected, the films are aligned and track reconstruction (volume tracks) is performed.

### 4.6.1 Emulsion alignment.

The mechanical accuracy of film piling in brick assembly is about 50-100 $\mu$m. Emulsion films are affected by environmental conditions, such as temperature and humidity, which may modify their original size; these effects must be taken into account as they could be the source of misalignments and deformations. To this extent, by computing a set of affine transformations (shift, rotation and expansion) relating track coordinates in consecutive films, it is possible to define a global reference system (hereafter referred to as *brick reference system*) prior to track reconstruction.

The film alignment is accomplished by means of two independent techniques. The first consists in the exposure of each brick to cosmic ray muons before the disassembling, as described in [32], the second one is the marking of brick with x-rays.

For the former technique, the following procedure is applied film by film: from a set of independent measurements in single emulsion films, an aligned volume is created through an iterative pattern matching procedure computing the parameters of the transformations

$$\begin{pmatrix} x^{brick} \\ y^{brick} \end{pmatrix} = \begin{pmatrix} a_{11} & a_{12} \\ a_{21} & a_{22} \end{pmatrix} \begin{pmatrix} x^{film} \\ y^{film} \end{pmatrix} + \begin{pmatrix} b_1 \\ b_2 \end{pmatrix} \tag{4.2}$$

where $x^{film}, y^{film}$ are single film track coordinates and $x^{brick}, y^{brick}$ are the corresponding aligned ones. A least square fit is applied after maximizing the number of matching pairs within predefined position and slope tolerances. The pairs are measured in three zones, typically chosen at the corners of the scanned area in order to maximize the lever arm to disentangle the contributions due to rotation and translation. This technique is time consuming due to the scanning time of the matching areas and to the computation time for the minimum finding.

The latter technique provides a much faster result, applying the mentioned affine transformation to the intersection points of the lateral x-ray marks. The acquisition and computation times are short and the speed gain is at least of 200%.

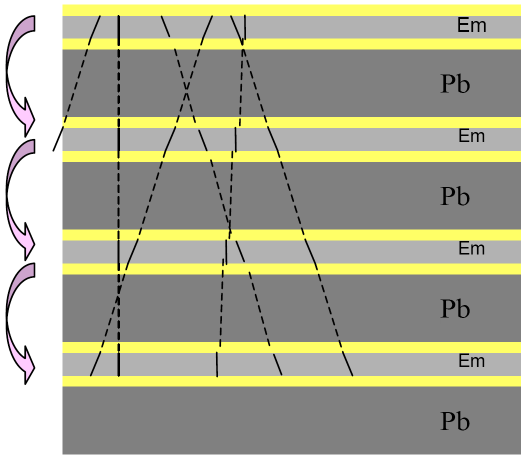


Figure 4.9: Follow-up of cosmic ray tracks through different emulsion plates and lead sheets used for local intercalibration of emulsions.

Once all plates are aligned, the track reconstruction algorithm finds and fits all the measured base-tracks of an emulsion film extending in both directions of the brick. In this way a number of connected base-tracks (not necessarily adjacent) forms a *volume-track*. The typical scanning procedure uses the *Scan-Back* method, following the volume track from the most down-stream plate up to the hypothetical stopping point which is supposed to be the vertex of the primary neutrino interaction. Once the vertex is found, a volume scan around that point is performed, to find other secondary tracks originated in the interaction, and following them in scan-forth method.

### 4.6.2 Off-line reconstruction

The off-line reconstruction available tools are either FEDRA (Framework for Emulsion Data Reconstruction and Analysis), an object-oriented tool based on C++ language developed in the Root framework [33], either AlphaOmega, a package of .NET executables specifically designed and optimized to perform the needed analysis operations on the output data.

The automatic microscope analysis provides the micro-tracks in the top and bottom layers of the emulsion film. The next step is to combine micro-tracks in pairs in order to obtain the base-tracks: micro-track pairs are projected across the plastic base. For each couple of micro-tracks a $\chi^2$ is calculated as

$$\chi^2 = \frac{1}{4}\left[\frac{(\theta_{xt}-\theta_{xB})^2}{\sigma_x^2} + \frac{(\theta_{xb}-\theta_{xB})^2}{\sigma_x^2} + \frac{(\theta_{yt}-\theta_{yB})^2}{\sigma_y^2} + \frac{(\theta_{yb}-\theta_{yB})^2}{\sigma_y^2}\right] \tag{4.3}$$

where $\theta_{xt(b)}$ and $\theta_{yt(b)}$ are the projections of respectively top (t) and bottom (b) micro-track angles in the $z-x$ and $z-y$ planes, $\theta_{xB}$ and $\theta_{yB}$ are the same

projections for the base-tracks (B) and $\sigma_x$ and $\sigma_y$ are the micro-tracks angular resolutions obtained for the distribution of the angular difference between micro-tracks and base-tracks.

If for one top micro-track more than one bottom candidate micro-track is found, more than one base-track can be reconstructed; in such a case the one with the smaller $\chi^2$ is selected.

# Chapter 5

# Results of scanning

This chapter presents the first neutrino interaction event in an OPERA brick fully reconstructed by the Padova scanning system. This result was an important milestone for the Padova group, and demonstrated that the whole acquisition system has been correctly set-up and is ready for real-life data analysis of OPERA bricks.

The analyzed brick is number `4554`, containing event `179673325CC`, already scanned at Napoli laboratory. The two measurements are in good agreement with each-other.

The present chapter briefly introduces the microscope image tuning and check-up, the *Scan-Back* procedure starting from the CS projection, the volume scan around the identified vertex, and finally the full event reconstruction.

## 5.1 Microscope tuning

The images of the emulsion grabbed by the CCD camera are sent to the Odyssey board hosted on the PC (see Section 4.4) where the cluster search is performed. The first operation on the acquired image is the so-called *flat field* subtraction. The flat field consists of one image grabbed outside of the emulsion, out of focus, which will be later subtracted from the grabbed frames. The image, mainly due to dust present on the camera CCD sensor, shows some dark spots, eventually interpreted by the DAQ software as clusters inside the emulsion. They need to be removed via software subtraction, otherwise they would lead to reconstruction of vertical fake tracks.

The second step is the image filtering, aiming to enhance the contrast between focused and unfocused grains (i.e. shadows of grains). Filtering is obtained by applying a convolution filter as reported in Section 4.2: each pixel output value is the result of a weighted sum including the neighborhood pixels input values.

The third step is the application of the so-called *equalization map*. In order to have an homogeneous cluster distribution inside the grabbed frames, an equaliza-

tion procedure is performed. It consists in defining several small cells inside the field of view of the camera. The surface of an emulsion is then scanned and the total number of clusters in each cell is counted with different applied thresholds. In order to keep the total number of clusters in each cell constant, a threshold map has to be used instead of an uniform threshold value. A threshold map obtained during our set-up is shown in Fig. 5.1. The uniformity of the map reflects the uniformity of the illumination of the field of view and of the camera sensor response. The dark corner indicates the need of a higher threshold in the corresponding area (∼70% of the central value).

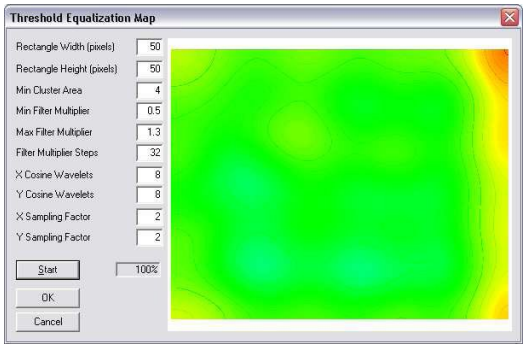


Figure 5.1: Equalization maps of threshold in the microscope view.

## 5.2 Brick location in OPERA

As described in Section 2.1.2, the neutrino interaction inside the OPERA target can be spotted using the Target Tracker and the Muon Spectrometer detectors. They provide valuable information on the location of the primary vertex interaction, more precisely in which ECC brick it occurred, and estimate the momentum of the product particles (primarily a muon), and providing hints on the kind of interaction, such as *Charged Current* (CC) or *Neutral Current* (NC).

Figure 5.2 shows the graphical reconstruction of the interaction given by the electronic devices. The gray squares represent the two module targets, in which the ECC bricks are stored, which are instrumented with the Target Tracer scintillator detectors, while the brown vertical bars represent the arms of the spectrometers, instrumented with the RPC gas detectors; at their sides the drift tubes of the Precision Trackers are shown as green vertical lines.

The upper and bottom part of the schema show the top-view and side-view of the experiment, respectively. It appears from the drawing that a $\nu_\mu$ event of Charged Current type occurred in first supermodule's target, and the originated muon went through the renaining of the detector. The momentum of the muon was estimated to be $p_\nu = 21.8$ GeV. Low hadronic activity is detected by the TT around the primary vertex.

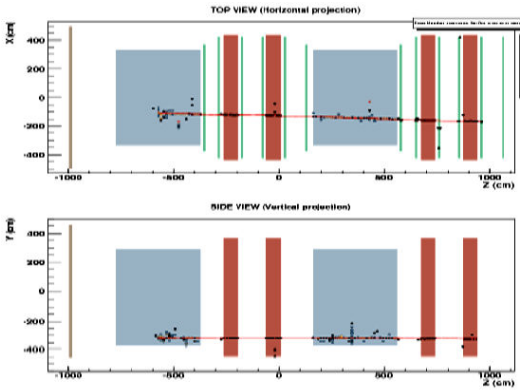


Figure 5.2: The event 179673325CC recorded by the electronic devices of OPERA.

Figure 5.3 shows a zoomed-in view of the Target Tracker recorded event. The green line represents the outgoing muon that originates from the vertex. The two black crosses mark the bricks extracted for development and microscope analysis.

## 5.3 TargetTracker to CS connection

The Changeable Sheets of the extracted bricks have been developed and scanned at LNGS. The extrapolation of the intersection point of the muon with the CS provided by the electronic devices is presented in Table 5.1 and is the starting point for the CS microscope scanning.

The CS doublet has been scanned around the predicted zone and the muon track has been found and identified around 1 mm from the projected position, with a good angular agreement. The results of the CS scanning performed at LNGS is presented in Table 5.2

| | |
|---|---|
| X position | 38.38mm |
| Y position | 31.22mm |
| $\theta_X$ angle | -0.023rad |
| $\theta_Y$ angle | -0.008 rad |

Table 5.1: Position of the outgoing track on the CS emulsion provided by the projection from the electronic devices, values are expressed in the emulsion coordinate system.

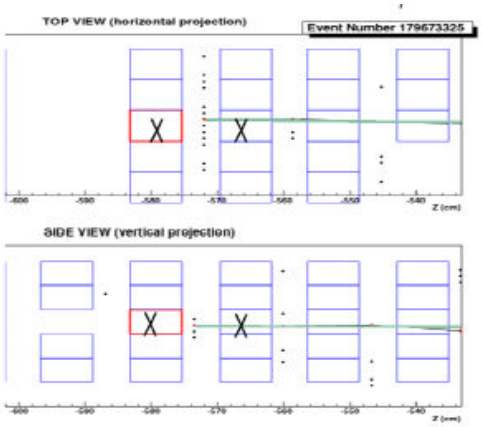


Figure 5.3: Information provided by the Target Tracker around the vertex brick. The top and side-view are presented; bricks are drawn as blue rectangles and the passing-through muon as a green line.

| | |
|---|---|
| $\Delta$X position | 720$\mu$m |
| $\Delta$Y position | -740$\mu$m |
| $\Delta\theta_X$ angle | 0.009rad |
| $\Delta\theta_Y$ angle | 0.043rad |

Table 5.2: Differences in position and angle between the TT-to-CS projection and the actual track found in the CS doublet.

## 5.4 Changeable Sheet to brick connection

The track found in the CS is then projected to the most downstream plate of the brick under inspection. The assumed distance of the emulsion from the CS doublet is $\Delta$Z = -4550 $\mu$m, where the minus sign is due to the OPERA convention for coordinates.

The analyzed brick presented 58 emulsion films, against the usual 57, due to an error in the production of the brick, with two emulsions inserted with no lead sheet in the between at positions 55 & 56. The track has been searched for on plate 58 around the projected position on a 1×1 cm$^2$ area.

The found track is within 60 $\mu$m from the projected position, and its parameters are shown in Table 5.3.

## 5.5 Scan-back and vertex finding

Once the track has been identified on the most downstream emulsion, it is followed upstream using the automated procedure called *Scan-Back* (SB), which is a

| | |
|---|---|
| $\Delta$X position | 52$\mu$m |
| $\Delta$Y position | -30$\mu$m |
| $\Delta\theta_X$ angle | 0.017rad |
| $\Delta\theta_Y$ angle | -0.007rad |

Table 5.3: Differences in position and angle between the CS-to-brick projection and the actual track found on plate 58.

database-driven standard process to localize the interaction points along its path in the brick.

The parameters to follow the tracks on each plate of the brick have been set in such a way that the candidate base-tracks satisfy the conditions shown in Table 5.4, to tollerate deviations due to multiple scattering in the lead sheets, and allow missing points (emulsions with no track found) due to inefficiencies or defects of the emulsion.

| | |
|---|---|
| Slope tolerance | $\pm$0.03 rad |
| Ang. tol. increase | 0.05$\times\theta$ (rad) |
| Position tolerance | $\pm$300$\mu$m |
| Pos. tol. increase per $\Delta$Z = 1500$\mu$m | 10$\times\theta$ $\mu$m/rad |

Table 5.4: Scan-back parameters used.

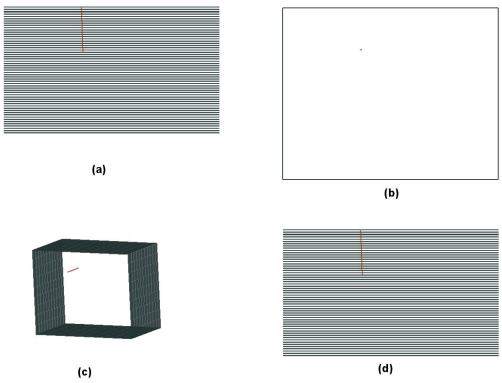


Figure 5.4: Results of the scan-back, showing the muonic track originating from the primary neutrino interaction vertex and traversing 22 emulsion films. Side-views (a-d), top-view (b) and 3D-view (c) are presented.

The track has been found on 22 consecutive emulsions within the presented cuts, with a stopping point between plate 36 and plate 37, as shown in Figure 5.4.

The residuals of the found base-tracks with respect to the projected ones is shown in Fig. 5.5, and are summarized in Table 5.5. These values are in agreement with previously performed measures on bricks exposed to test-beam pions but without interleaved lead plates. The residuals show no dependance on the plate number (see Fig. 5.6), so that systematic effects can be excluded for the Scan-Back. Better resolutions could be achieved with a local intercalibration with cosmic rays around the interaction point on each plate.

| |
|---|
| $\sigma_X = 12\mu$m |
| $\sigma_Y = 14\mu$m |
| $\sigma_{\theta_X} = 0.0033$ rad |
| $\sigma_{\theta_Y} = 0.0058$ rad |

Table 5.5: Summary of scan-back track precisions from residuals against projected tracks.

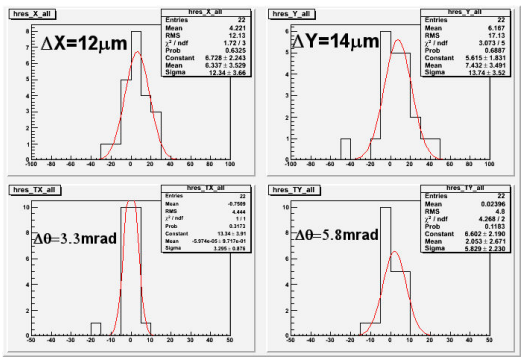


Figure 5.5: Residuals of the scan-back for the measured tracks against the projections from the previous emulsion.

## 5.6 Event reconstruction

The final step of the analysis after the identification of the stopping point is the volume scan of the emulsions around the candidate vertex. The volume size is chosen in order to minimize the scanning time without losing efficiency in the event recognition. The volume should be large enough to allow the reconstruction of primary tracks of reasonably high momentum close to the vertex. A study conducted by Naples group demonstrated that in case of charged current events, with the same simulated efficiency, a volume of 11 plates (5 upstream and 5 downstream of the stopping point plate) over an area of $5\times5$ mm$^2$ does not significantly reduce the event recognition power which is $(97\pm1)\%$ with respect to the full brick volume

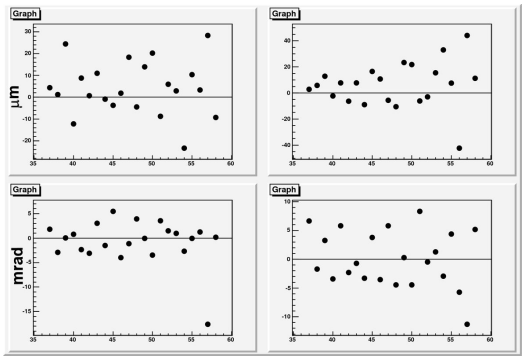


Figure 5.6: No systematic effect is visible looking at the residuals as a function of the emulsion position.

reconstruction[39]. For our analysis we executed the scan of a $5 \times 5$ mm$^2$ on 1 upstream and 5 downstream plates with respect to the supposed vertex.

The vertex reconstruction algorithm is based on the preliminary selection of tracks pairs with a small *impact parameter* (IP) and satisfying some topological criteria. Starting from track pairs, the $n$-prong vertices are constructed using a Kalman Filter (KF) procedure. The final vertex selection criteria is based on the $\chi^2$ probability of the vertex defined by the KF.

The result of our analysis is show in Figure 5.7. A muon and an hadronic track are recognized, with 0.6 $\mu$m and 6.7 $\mu$m impact parameters respectively. Further details are reported in Table 5.6.

| | |
|---|---|
| Muon IP | 0.6$\mu$m |
| Muon $\theta_X$ | -0.0318 rad |
| Muon $theta_Y$ | 0.0020 rad |
| hadronic IP | 6.7$\mu$m |
| hadronic $\theta_X$ | -0.397 rad |
| hadronic $theta_Y$ | -0.583 rad |

Table 5.6: The parameters of the reconstructed tracks originating from the primary neutrino vertex.

The matching of the muonic track reconstructed in the volume scan with the tracks of the scan-back is shown in Figure 5.8. A further investigation around the interaction vertex was the selection of single base-tracks pointing to the vertex with a small impact parameter (IP<20 $\mu$m) and a considerable number of grains (N>22). These tracks are probably due to soft (i.e. low energy) nuclear fragments that are completely stopped by the first downstream lead plate, as shown in Fig. 5.9.

The current analysis has been obtained in the very last part of my Ph.D. period

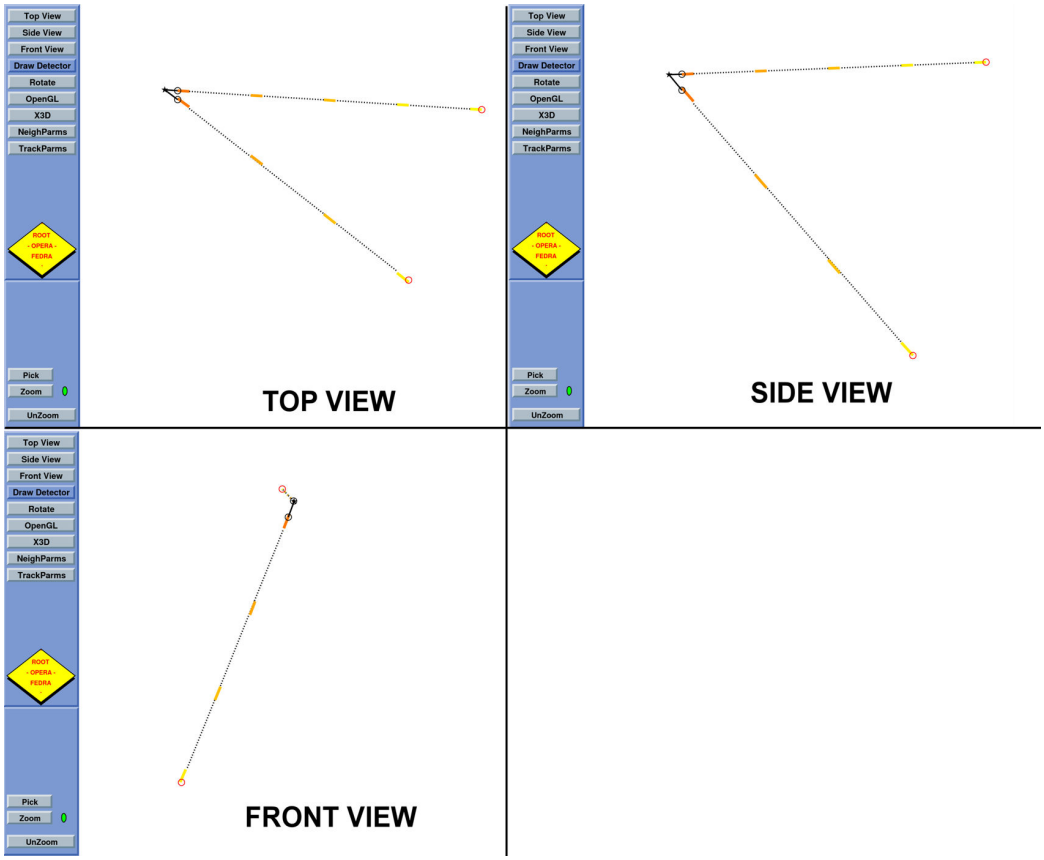


Figure 5.7: Event reconstruction of the neutrino interaction vertex.

between November 2007 and January 2008, it still needs some improvements, but it can already be considered fully satisfactory in the perspective of the OPERA data-taking that will start this year, which will require the Padova group to scan on average 1 brick per week.

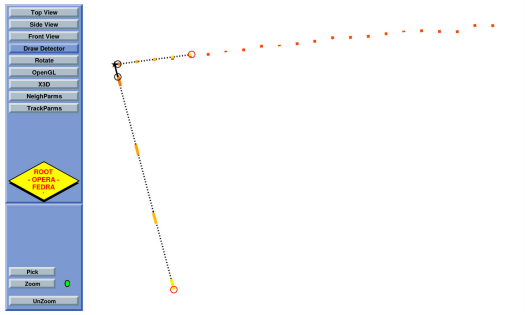


Figure 5.8: Matching of tracks reconstructed with volume scan around the vertex and the track followed during the scan-back procedure.

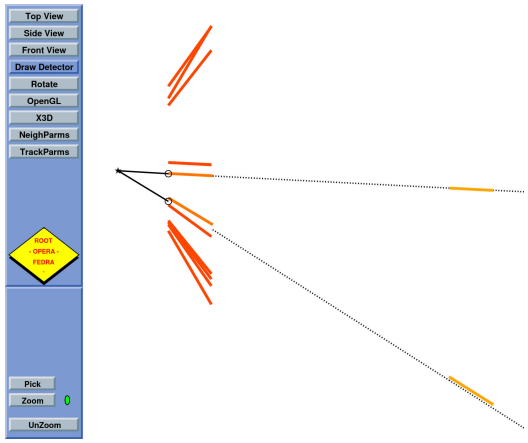


Figure 5.9: Selection of single base-tracks in plate 37 pointing to the interaction vertex (side-view).

# Chapter 6

# Conclusions

The OPERA experiment aims at the confirmation of $\nu_\mu \rightarrow \nu_\tau$ oscillations through the direct observation of $\nu_\tau$ neutrinos in an initially almost pure $\nu_\mu$ beam produced at CERN. The OPERA experiment is a kTon-two-supermodule detector with a target of lead-emulsion sandwiched in "bricks" and a magnetic spectrometer. The large amount of nuclear emulsions used in OPERA (about 7 milion 10-cm$^2$ films) requires automated developing in large-scale and fast automatic scanning microscopes with high speed and accuracy. This thesis covers both items, to which I have contributed in the years of the Ph.D. work.

OPERA installation of bricks started in April 2007 and is expected to end in June 2008. Meanwhile the first physics run was available from CERN in October 2007, when 38 events of $\nu_\mu$ interaction in lead where collected.

The first major project I have been working on has been the design and realization of high-level control software for the automatic development lines at Gran Sasso laboratories. Such project required a flexible interface for the machine, which has been achieved using a modular software approach, with an architecture based on the open standard for automation control called OPC. On top of that, the scheduling manager is able to safely handle any number of bricks simultaneously on the lines, finding the best way to provide a high-quality uniform development. The different independent layers in which the program is structured provide a stable and easy-to-manage form to the whole project.

The second important project I've been working on has been the Padova scanning station at Legnaro laboratories. I've contributed at installation, set-up and operation of the microscope and the whole scanning system. The main goal of the PhD work was to successfully scan a real OPERA brick (corresponding to one of the 38 events), performing the scan-back and vertex reconstruction. The obtained results are still partially preliminary since they have been obtained very recently between November 2007 and January 2008; they are nevertheless very promising.

With this analysis the Padova group has identified its first OPERA $\nu$ event, demostrationg that the whole scanning system has been installed, configured and operated correctly, au-pair with all the other laboratories of the collaboration.

The Padova scanning laboratory is able to scan and reconstruct real-life OPERA events, and so it will do for at least the next 5 years.

# Bibliography


[1] W. Pauli, letter to a physicist's gathering at Tubingen, December 4, 1930. Reprinted in *Wolfgang Pauli, Collected Scientific Papers*, ed. R. Kronig and V. Weisskopf, Vol. 2, p. 1313 (Interscience: New York, 1964).

[2] C.L. Cowan, Jr., F. Reines, F.B. Harrison, H.W. Kruse and A.D. McGuire, *Detection of the Free Neutrino: A Confirmation*, Science **124, 103** (1956).

[3] D.H. Perkins, Introduction to High Energy Physics, Third Edition, Section 7.2; Addison-Wesley Publishing Company.

[4] S.L. Glashow, Nucl. Phys., **22** (1961) 579;
S. Weinberg, Phys. Rev. Lett. **19** (1967) 1264;
A. Salam, Proceedings of the 8th Nobel Symposium on *Elementary particle theory, relativistic groups and analyticity*, (1968), ed. Swartholm, Almquist and Wiksells, p.367.

[5] B. T. Cleveland *et al.*, "Measurement of the solar electron neutrino flux with the Homestake chlorine detector," Astrophys. J. **496** (1998) 505.

[6] (SNO Coll.), Q. R. Ahmad et al., Phys. Rev. Lett. **87** (2001) 071301.

[7] (Kamiokande Coll.), K. S. Hirata et al. , Phys. Lett. **B280** (1988) 146; Phys. Lett. **B280** (1992) 146 ; Y. Fukuda et al., Phys. Lett. **B335** (1994) 237.

[8] B. Pontecorvo, Zh. Eksp. Teor. Fiz. **33** (1957) 549; Zh. Eksp. Teor. Fiz. **34** (1958) 247; Zh. Eksp. Teor. Fiz. **53** (1967) 1717.

[9] R. N. Mohapatra *et al.*, "Theory of neutrinos," arXiv:hep-ph/0412099.

[10] A. A. Penzias and R. W. Wilson, "A Measurement of excess antenna temperature at 4080-Mc/s," Astrophys. J. **142** (1965) 419.

[11] (MACRO Coll.), M. Ambrosio et al., Phys. Lett. **B517** (2001) 59; Phys. Lett. **B478** (2000) 5.

[12] M. Gell-Mann, P. Ramond and R. Slansky, *Supergravity*, ed. D. Freedman and P. van Nieuwenhuizen (North-Holland, Amsterdam, 1979), p. 315;

T. Yanagida, *Proceedings of the Workshop on Unified Theory and Baryon Number in the Universe*, ed. O. Oswada and A. Sugamoto (Japan, 1979); R. Mohapatra and G. Senjanovic, Phys. Rev. Lett. **44** (1980) 912; Phys. Rev. Lett. D **23** (1981) 165.

[13] A. Faessler and F. Simkovic, "Double beta decay," J. Phys. G **24** (1998) 2139 [arXiv:hep-ph/9901215].

[14] C.K. Jung, C. McGrew, T. Kajita and T. Mann, Ann. Rev. Nucl. Part. Sci. **51** (2001) 451.

[15] F. Boehm and P. Vogel, *Physics of Massive Neutrinos*, Cambridge Univ. Press, (Cambridge 1987).

[16] G. Acquistapace et al., "The CERN neutrino beam to Gran Sasso (NGS)", Conceptual Technical Design, CERN 98-02 and INFN/AE-98/05 (1998).

[17] ASHRAE, "Standard 34-2007, Designation and Safety Classification of Refrigerants (ANSI Approved)", ISSN 1041-2336.

[18] American Chemical Society, "Chemical abstracts", ISSN 0009-2258.

[19] H. Pessard [OPERA Collaboration], "The OPERA experiment,", Invited talk at 32nd International Conference on High-Energy Physics (ICHEP 04), Beijing, China, 16-22 Aug 2004. Published in "Beijing 2004, ICHEP 2004, vol. 1" 299-303.

[20] L. S. Esposito, *Study of electron identification in the emulsion cloud chambers of the OPERA experiment*, PhD Thesis, Bologna (2005).

[21] B. Van de Vyver and P. Zucchelli, Nucl. Instr. Meth. **A385** (1997) 91.

[22] (OPERA Coll.), M. Guler et al. *Experimental proposal*, CERN-SPSC-2000-028;

[23] CNGS project: http://proj-cngs.web.cern.ch/proj-cngs/; (OPERA Coll.), M. Guler et al. CERN-SPSC-2001-025.

[24] L. Arrabito et al., Nucl. Instrum. Methods **A568** (2006) 578.

[25] Tsai-Chu Determination of Distortion Vector in Nuclear Emulsion il Nuovo Cimento, Vol. 5.5, (1957)1128.

[26] S. Aoki et al., Nucl. Instr. Meth. **B51** (1990) 466.

[27] S. Aoki, Nucl. Instr. Meth. **A473** (2001) 192.

[28] G. Rosa et al., Nucl. Instr. Meth. **A394** (1997) 357.

[29] N. Armenise et al., Nucl. Instrum. Meth. **A551** (2005) 261.

[30] W.J. Smith, Modern optical engineering, the design of optical systems, Third Edition, McGraw-Hill (2000).

[31] M. De Serio et al., Nucl. Instrum. Meth. **A554** (2005) 247.

[32] E. Barbuto et al., Nucl. Instrum. Meth. **A525** (2004) 485.

[33] V. Tioukov et al., Nucl. Instrum. Meth. **A559** (2006) 103.

[34] "Design Patterns: Elements of Reusable Object-Oriented Software", Erich Gamma, Richard Helm, Ralph Johnson, and John Vlissides (1995).

[35] C. Sirignano, "R&D on OPERA ECC:studies on emulsion handling and event reconstruction techniques", PhD Thesis, Salerno University, AA (2005).

[36] G. Rosa et al. "Automatic Development of OPERA emulsion film", 2004.

[37] Walter H. Barkas, Nuclear research emulsion (1963) Academic Press, New York and London.

[38] G. Romano, "Emulsioni Nucleari" (1978), Rome University.

[39] L. Consiglio, "Algorithms for the analisys of neutrinos in the OPERA-like Emulsion Cloud Chambers", PhD Thesis, Bologna University,(2006)

[40] L. Landau, Nucl. Phys. **3** (1957) 127.

[41] T.D. Lee and C.N. Yang, Phys. Rev. **105** (1957) 1671.

[42] E. Majorana, Nuovo Cim. **14** (1937) 171.

[43] S. Eidelman et al. (Particle Data Group), Phys. Lett. B **592** (2004) 467.

[44] B. Kayser, *Neutrino physics as explored by flavor change* in K. Hagiwara et al. (Particle Data Group), Phys. Rev. D **66** (2002) 392.

[45] L. Wolfenstein, Phys. Rev. D **17** (1978) 2369;

[46] Z. Maki, M. Nakagawa and S. Sakata, Progr. Theor. Phys. 28 (1962) 870.

# Acknowledgements

I would like to acknowledge for the huge help, guidance and encouragement during my Ph.D. work professors Luca Stanco and Riccardo Brugnera. I thank their positive influence and fruitful collaboration which resulted in a great professional and personal enrichment for me.

I also acknowledge professor Gianni Rosa and Elio Buccheri for the invaluable help at the automated development project.

My deepest gratitude goes to Andrea Longhin with whom I've shared endless days solving problems at the microscope and who has helped me out in countless situations.

A big thank you for the whole Padova group, which supported me in all these years, Antonio Bergnoli, Alessandro Bertolin, Robert Ciesielki, Flavio Dal Corso, Stefano Dusini, Alberto Garfagnini.

I acknowledge the huge number of wonderful colleagues of the OPERA experiment that helped me out during all this time and made me enjoy my time in all situations. I will list them in strictly random order, apologizing to the ones that I am forgetting: Mario Spinetti, Lucia Votano, Adriano Di Giovanni, Natalia Di Marco, Nicola D'Ambrosio, Luigi *Luillo* Esposito, Maurizio Ventura, Sandro Mengucci, Alessandro Paoloni, Francesco Terranova, Donato Di Ferdinando, Massimiliano Sioli, Gabriele Sirri, Andrea Schembri, Alessandro Pelosi, Saverio Simone, Alessandra Pastore, Michela Ieva, Lucia Consiglio, Marilisa De Serio, Cristiano Bozza, Chiara Sirignano, Romolo Diotallevi, Aldo Andriani.

Last but not least I thank my parents Marilena and Maurizio, my brother Luca, my grand parents Yvonne and Onesto for being always close to me in joyful and in painful moments. My dearest friends Marco, Ernesto, Filippo, Vittorio, Daniele, Agata who might live far away, but are always at my side.

To Magdalena, always in my heart.